Towards predicting failure modes in multi-material extrusion-based additive manufactured PETG/TPC structures

Christoph Waly [a], Vasco D.C. Pires [b], Philipp Beier [c], Sandra Schulnig [d], Ivica Duretek [c], Martin Pletz [b], Florian Arbeiter [a,*]

[a] Institute of Materials Science and Testing of Polymers, Technical University of Leoben, Otto Gloeckel-Strasse 2, 8700 Leoben, Austria
[b] Institute of Designing Plastics and Composite Materials, Technical University of Leoben, Otto Gloeckel-Strasse 2, 8700 Leoben, Austria
[c] Institute of Polymer Processing, Technical University of Leoben, Otto Gloeckel-Strasse 2, 8700 Leoben, Austria
[d] ADMiRE Research Center, Carinthia University of Applied Sciences, Europastrasse 4, 9524 Villach, Austria

ABSTRACT

The presence of defects in Fused Filament Fabrication (FFF) multi-material components can lead to various failure mechanisms, mainly depending on the interface quality between adjacent materials. This study investigates the predictability of crack deflection or penetration using two established criteria from Cook & Gordon (C&G) and He & Hutchinson (H&H). Samples are printed from glycol-modified poly(ethylene terephthalate) (PETG) and a compliant thermoplastic elastomer on copolyester basis (TPC), where TPC serves as a compliant interlayer (IL) within a PETG matrix. To evaluate the stress-based C&G model, tensile tests are conducted on mono- and multi-material specimens. The fracture toughness of the TPC IL is determined using the Essential Work of Fracture approach. Interface fracture toughness between PETG and TPC is assessed using a stiffness drop technique combined with a finite element model, which applies the *J*-integral method. Two IL thicknesses of 0.3 and 0.8 mm are tested. The results from mechanical testing show that IL thickness does not significantly affect interface strength, but show that the choice of specimen geometry plays a key role regarding fracture behavior. Fracture tests reveal that increasing IL thickness enhances the macroscopical interface fracture toughness, although the TPC IL fracture toughness itself remains unaffected. The C&G criteria prove unreliable due to high nonlinearity, mainly due to the TPC layer. In contrast, the H&H criteria correctly identify the failure mode. Nevertheless, further investigations are necessary to validate the given transition value, as the toughness difference between the TPC IL and the interface is too large for conclusive interpretation.

1. Introduction

The printing of dissimilar materials via multi-material additive manufacturing (MMAM) offers remarkable advantages over single- or mono-material additive manufacturing (AM). Originally developed to address the limitations of mono-material printing – most notably the comparatively lower mechanical performance of AM parts relative to conventionally manufactured components (e.g., injection molded parts [1]) - MMAM today mainly targets enhanced component functionality [2–6], a reduction in part count, and optimized assembly [7]. In addition, MMAM enables the selective combination of materials with different mechanical, optical, electrical, and thermal properties, among others. This not only expands design freedom but also holds potential for applications in critical sectors such as aerospace (e.g., for lightweight

structures [8]), electronics (e.g., for soft robotics and actuators [9], printed circuit boards [10]), biomedicine (e.g., for drug delivery, tissue engineering, etc. [11]), as well as construction by enhancing damage tolerance [12–15] in load-bearing structures. However, the extensive versatility of MMAM components is well-documented, as demonstrated in the recent review by e.g. Khan et al. [16] or Nazir et al. [17]. Despite the wide array of modern AM techniques, such as material jetting and vat photopolymerization, material extrusion technologies, particularly the fused filament fabrication (FFF) process, remain among the most significant and widely adopted methods. This prominence is largely attributed to their ability to print a variety of more application-related materials, ease of use, and cost efficiency, making them an indispensable tool in the realm of advanced manufacturing.

Regardless of the number of materials integrated into a single component, the manufacturing process follows a layer-by-layer

Nomenclature

σ_i	interface strength
σ_m	strength of the mono-material in general
$\sigma_{m,\,Matrix}$	strength of the matrix mono-material
$\sigma_{m,\,IL}$	strength of the interlayer mono-material
E_m	Young's modulus of the mono material in general
$E_{m,\,Matrix}$	Young's modulus of the matrix mono-material
$E_{m,\,IL}$	Young's modulus of the interlayer mono-material
ν_m	Poisson's ratio in general
$\nu_{m,\,Matrix}$	Poisson's ratio of the matrix mono-material
$\nu_{m,\,IL}$	Poisson's ratio of the interlayer mono-material
Π_i	interface fracture toughness
Π_{IL}	fracture toughness of the interlayer material
G_d	energy release rate for a deflecting crack
G_p	energy release rate for a penetrating crack
α	first Dundurs parameter
W_f	overall fracture energy
W_S	energy necessary to create new surfaces
W_{pl}	energy dissipated for plastic deformation in the volume around the fracture zone
w_e	essential work of fracture
w_p	non-essential work of fracture
w_{sf}	specific fracture energy
β	shape factor
a_0	initial crack length
L_{th}	theoretical ligament length
L_{real}	real ligament length
W	specimen width
F_c	critical crack initiation force
F_{max}	maximum force
$F_{c,\,optical}$	crack initiation force detected by digital image correlation

$\rho_{Filament}$	density of the neat PETG/TPC filament
ρ_{FFF}	density of the printed PETG/TPC structure
r^2	coefficient of determination
n	sample runs
AM	additive manufacturing
MMAM	multi-material additive manufacturing
FFF	fused filament fabrication
C&G	Cook & Gordon
H&H	He & Hutchinson
LEFM	linear elastic fracture mechanics
PS	plane stress
PE	plane strain
DCB	double-cantilever beam
SENB	single-edge notched bending
DENT	double-edge notched tension
EWF	essential work of fracture
DIC	digital image correlation
MFR	melt flow rate
IL	interlayer
X	interlayer thickness (=0.3 or 0.8 mm)
PETG	glycol-modified poly(ethylene terephthalate)
TPC	thermoplastic elastomer on copolyester basis
TPU	thermoplastic polyurethane-based elastomer
PMMA	poly(methyl methacrylate)
PLA	polylactic acid
PA12	polyamide 12
ABS	acrylonitrile butadiene styrene
PP	polypropylene
PEEK	polyether-ether-ketone
PET	poly(ethylene terephthalate)
LLDPE	linear low-density polyethylene
EVOH	ethylene-(vinyl acetate) copolymer

deposition of individual strands. These strands and layers bond through a combination of wetting, neck formation, and molecular diffusion until the final structure is formed [18]. In mono-material AM, this deposition is executed by a single extrusion head, whereas in MMAM, multiple extrusion heads [16,19] are utilized, or material switching occurs during the printing process [12]. Due to the diverse range of process parameters involved in strand and layer deposition within the FFF process, numerous interfaces are inherently formed [20]. The strength of these interfaces depends on the extent of wetting, neck formation, and diffusion, which vary based on the process conditions [18], as shown e.g. in glycol-modified poly(ethylene terephthalate) (PETG) in Refs. [21, 22]. This inherent characteristic presents both a challenge (spontaneous catastrophic failures) and an opportunity (increase in damage resistance) in FFF-printed structures.

During a component's service life, cracks may develop. Depending on the mechanical and/or fracture properties of the interface and its surrounding material, these cracks may either deflect along the interface, known as crack deflection [23–25], or penetrate through it, known as crack penetration [25,26]. This phenomenon can be strategically leveraged to control crack propagation and enhance damage tolerance. If an interface is surrounded by a single material, its properties can be deliberately tailored through process-controlled parameters such as printing speed and extrusion temperature [27]. Alternatively, a material-controlled approach can be adopted by printing dissimilar materials around the interface. This often involves a deliberate mechanical mismatch - typically a combination of compliant and stiff materials - to influence crack behavior, as shown e.g., by Waly et al. [12] in MMAM Charpy samples made of PETG and a thermoplastic elastomer on copolyester basis (TPC), as a stiff and compliant constituent, respectively. Nevertheless, many material combinations inherently

exhibit weak interfaces due to their limited chemical and thermodynamic affinity, often resulting in insufficient interfacial adhesion [17], which creates the possibility for a growing crack to deflect into the interface. Consequently, a wide range of strategies and approaches have been developed to modify the interface between dissimilar materials. These include techniques such as mechanical interlocking [28,29] and various surface treatment methods [30], aimed at enhancing interfacial bonding. However, a significant research gap remains regarding the reliable prediction of when and under which conditions cracks in dissimilar FFF multi-material structures are more likely to deflect along an interface or penetrate subsequent layers. Addressing this gap is the primary objective of this study.

The topic of failure mode prediction is not being addressed for the first time in this study; rather, it has been a subject of scientific investigation for quite some time. An initial description was provided by Cook & Gordon (C&G) [31] in the 1970s, where they discovered that cracks are more likely to deflect if the theoretical strength of the interface is less than or equal to 20 % of the theoretical strength of the material following the interface. This criterion is further referred to as the stress-based approach. Later, He & Hutchinson (H&H) [25,32] adopted a fracture mechanics approach (energy-based approach) to failure mode prediction. They published findings indicating that cracks are more prone to deflection when the ratio of the fracture toughness of the interface to the fracture toughness of the material following the interface is less than or equal to 25 %, in the case of similar materials across the interface. Both concepts, in their simplest form, have been widely applied across various material classes - including ceramics/ceramic composites [33–35], metals/metal composites [36], and polymers/polymer composites [37–41] - to describe and predict failure modes and have been continuously refined over the years [42]. However, the results

regarding the application and its suitability for failure mode prediction of the two mentioned criteria are quite diverse. Focusing on polymers and polymer composites, Alam et al. [38] did not observe agreement between their results in bonded poly(methyl methacrylate) (PMMA) and the H&H criterion. Similarly, Lee et al. [37] conducted experiments on PMMA and found a significant deviation from the proposed 0.25 threshold by H&H, reporting a ratio of 0.64. In contrast, Jia and Wang [39] observed consistency with the H&H criterion in inkjet-printed brick-and-mortar structures. In a previous study, Waly et al. [22] investigated failure mode prediction in various polymers and observed that the H&H criterion did not align with the failure modes observed in their validation samples. They highlighted potential issues related to the nonlinear material behavior and challenges in crack initiation. Unlike the C&G criterion, the H&H approach assumes that a crack has already impinged on an interface. In the contrary, the C&G criterion, which does not require this condition, demonstrated good agreement with their experimental findings. Building on this work, they conducted additional strain rate-dependent studies on PETG and again observed good alignment with the C&G criterion, provided that the assumptions regarding nonlinearity and plastic zone size were, according to linear elastic fracture mechanics (LEFM), not significantly violated [21]. In brief, both criteria were originally developed for brittle material behavior and are based on LEFM assumptions. However, while the H&H criterion requires that the crack has already impinged on the interface, the C&G criterion does not consider this as a determining factor [25,31,32].

Despite the simplicity of these two criteria (in their most basic form), accurately determining interface properties remains a challenge, especially for the H&H criteria. This is reflected in the limited number of reports on characterization methods available in the literature. Despite significant interest from both academia and industry, there are still very few studies focused on dissimilar materials. In most studies, basic stress-strain methods, such as tensile testing [43–45] on bi-material samples, have been employed. However, only a limited number of studies focus on fracture mechanics-based characterization techniques to quantify the interface adhesion strength of stiff-to-compliant material combinations. Yavas et al. [46] conducted fracture mechanics investigations on printed double-cantilever beam (DCB) specimens composed of polylactic acid (PLA) and a thermoplastic polyurethane-based elastomer (TPU). Under Mode I loading, they reported a fracture toughness of approximately 48 ± 10 J/m^2 while neglecting the nonlinearity of TPU. Building on the prior work of Rabbi et al. [47], Stiller et al. [48] investigated the single-leg bending test for stiff/compliant material combinations of polyamide 12 (PA12) and TPU. While this test appears to be a viable alternative or complement to the DCB test for stiff material pairings, it seems unsuitable for stiff/compliant combinations, as its underlying assumptions are based on the principles of LEFM, raising questions about the validity of the evaluation. Pakhare et al. [49] conducted fracture mechanics studies on FFF-manufactured acrylonitrile butadiene styrene (ABS) and TPU DCB specimens. To address the nonlinear behavior of TPU and the blunting issue of the crack tip at the interface, they developed a finite element model to determine fracture toughness using the *J*-integral approach. Their findings indicated that fracture toughness was independent of initial crack length but influenced by TPU layer thickness. Thicker TPU interlayers (IL) led to increased fracture toughness due to the formation of larger damage zones ahead of the crack tip.

The investigations in this study are broadly divided based on the existing research gaps. First, already established characterization methods for comprehensively assessing the mechanical and fracture mechanical properties of both bulk materials and interfaces in multi-material FFF printing will be presented and discussed in detail. Second, the applicability of the C&G and H&H criteria in predicting the failure mode of multi-material FFF-manufactured PETG/TPC structures will be evaluated. Building upon the findings of this and two preceding studies [21,22], recommendations for selecting an appropriate failure criterion will be proposed and thoroughly analyzed.

2. Experimental

To assess the suitability of predicting crack propagation (crack deflection vs. crack penetration) using the two aforementioned criteria (C&G and H&H), an experimental procedure was established in advance, as schematically illustrated in Fig. 1. Specifically, crack propagation in a fracture mechanical single-edge notched bending (SENB) specimen under three-point bending was examined. Subsequently, the actual failure behavior was compared with the predictions of the criteria to identify potential correlations or discrepancies.

As illustrated in Fig. 1, crack propagation in a multi-layered SENB specimen with a stiff outer matrix and an embedded compliant IL is to be investigated. For the C&G criterion, it is necessary to determine the strength of the interface, σ_i, as well as the strength of the mono-material adjacent to the interface, $\sigma_{m, IL}$, which in this case refers to the compliant IL material.

For the H&H criterion, the first step is to determine the threshold at which crack deflection theoretically transitions to crack penetration. This requires knowledge of Young's modulus, E_m ($E_{m, Matrix}$ & $E_{m, IL}$), and Poisson's ratio, ν_m ($\nu_{m, Matrix}$ & $\nu_{m, IL}$), of the mono-matrix and IL material. Subsequently, the interface fracture toughness, Π_i, and the fracture toughness of the mono-material adjacent to the interface, Π_{IL}, has to be determined. As with the C&G criterion, Π_{IL} corresponds to the fracture toughness of the compliant IL material. However, it is important to note, that this additional step is not required for the C&G model, as the threshold remains constant at 0.2, making it independent of the materials used (whether a mechanical property mismatch is present or not).

To ensure the comprehensibility of this study, the materials used are first presented, followed by an explanation of the printing strategy, which is of particular importance, as identical conditions within the printed materials and the interfaces must be ensured for both the specimens and the SENB validation samples. This is followed by the experimental tests to determine strength and fracture toughness, culminating in the final validation tests.

2.1. Materials

Within this study, two materials with distinct mechanical properties were utilized. For the stiff matrix material, one of the most widely used filament material, PETG, was used which has been extensively investigated in previous studies [21,22,50–53]. However, in within study, the PETG was obtained from Prusa Polymers (Prague, Czech Republic) under the trade name Prusament PETG Jet Black. In contrast, TPC as a compliant soft IL was selected due to its chemical affinity with PETG, as both materials are based on copolyester. The TPC used (FlexiFil™ White) was sourced from Formfutura BV (Nijmegen, the Netherlands). Both materials are commercially available as filaments for FFF with a diameter of 1.75 mm. According to the manufacturers' datasheets [54, 55,], the E_m ratio (PETG/TPC) is approx. 16 (1500/95 MPa), highlighting the difference in their mechanical properties. Prior to printing, however, the materials underwent thorough pre-drying for at least 24 h at 40 °C.

2.2. Printing strategy and sample fabrication

All specimens were fabricated using an Original Prusa i3 MK3S+ FFF printer (Prusa Research, Czech Republic), which was equipped with a Multi-Material Unit MMU2S (Prusa Research, Prague, Czech Republic). The MMU2S works according to the principle of material switching during the printing process whose detailed functionality can be found, e. g., in Ref. [12]. The print head was fitted with a 0.4 mm brass nozzle. After slicing the files with PrusaSlicer software, version 2.9.0 (Prusa Research, Prague, Czech Republic), a series of specimens, as shown in Fig. 2, were printed onto a Polyetherimide-coated steel plate to ensure first-layer adhesion and minimize warping. It should be noted that the specimens shown in Fig. 2 are already oriented on the build platform as
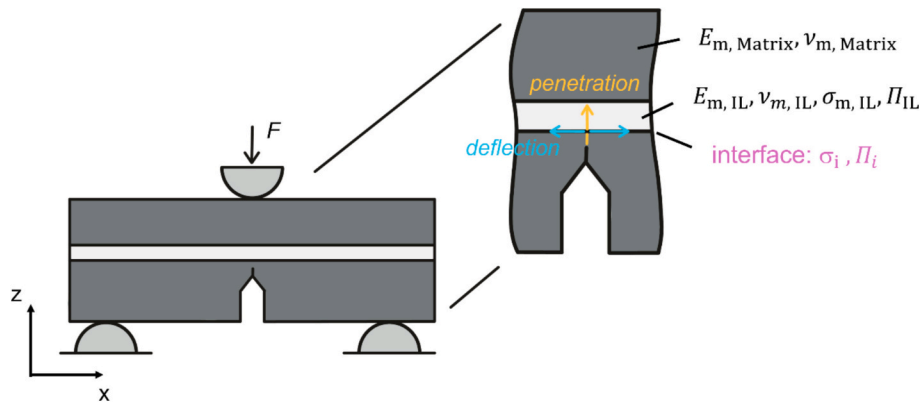
Fig. 1. Schematic overview of the mechanical/fracture mechanical parameters determined to assess the applicability of the Cook & Gordon (C&G) and He & Hutchinson (H&H) criteria for failure mode prediction in multi-material printed components.
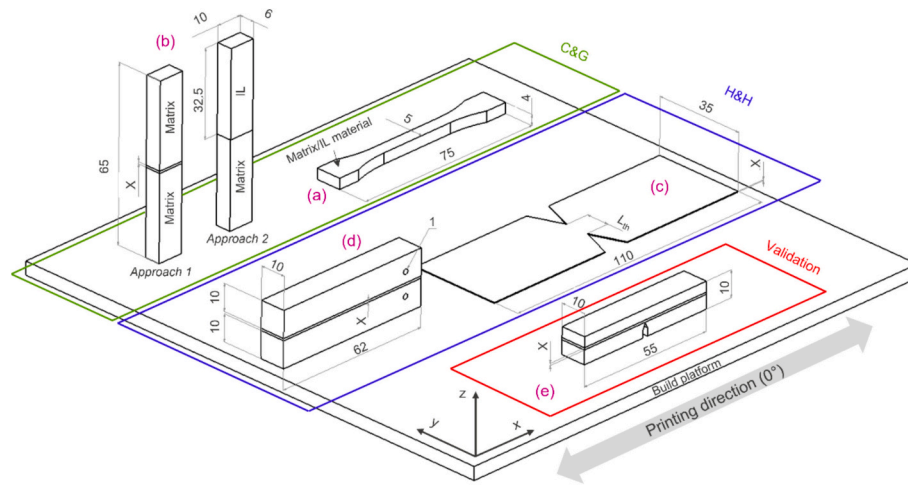
Fig. 2. Printing strategy and selected dimensions of the specimens used for the various investigations. The samples are oriented on the build platform as in their final printed state. All dimensions are given in mm.

in their final printed state.

Samples were printed unidirectionally (0°) with a layer height of 0.1 mm, a printing speed of 30 mm/s, a 100 % infill, an extrusion multiplier of one, a fan speed of 60 %, and a nozzle temperature of 240 °C, regardless of the material. It is also important to note at this point, that build platform heating was deactivated for all prints, meaning that the materials were processed under ambient conditions (~23 °C). This approach was chosen to eliminate any influence of build platform temperature on the initial few layers and morphology, as shown, e.g., in Refs. [21, 56]. This is particularly important when thinner structures are printed directly on the build platform, such as samples (a) and (c). Using a conventional approach with elevated build platform temperatures would, depending on the selected material, increase chain mobility and thus promote a more homogeneous and denser microstructure, which in turn could alter the mechanical properties. To overcome these influences, the chosen printing strategy was applied in order to maintain consistent conditions at the crack tip of the validation specimens and across all other samples, thereby enabling meaningful and comparable assessments.

For the investigation of the C&G criterion, two types of specimens were printed, as shown in Fig. 2. To determine the strength of the mono-materials ($\sigma_{m, IL}$ and $\sigma_{m, Matrix}$), tensile specimens were printed based on DIN EN ISO 527-2/Type 1BA [57] with a thickness of 4 mm (Sample a). The second set of specimens was used to determine σ_i (Sample b). In this case, tensile specimens without shoulders were selected with dimensions of $(10 \times 6 \times 65)$ mm³. This choice of specimen is primarily

based on a previous study [21] and on several recommendations by Sola et al. [58]. It was observed that the thickness of the specimens has a strong influence on σ_i. If the specimens are too thin, edge effects and instabilities as well as thermal conditions during strand deposition can affect σ_i; if they are too thick, out-of-plane failure can occur due to possible shear stresses, which in turn can distort the results. For this reason, a thickness of 6 mm was chosen, as this falls within a range where σ_i remains constant, thereby ensuring comparable conditions to the validation specimens. Moreover, two different approaches were employed. In Approach 1, an IL, marked as X in Fig. 2 (Sample b), was printed between the stiff matrix material. The X consistently indicates the thickness of the IL material throughout Fig. 2. In this study, two different IL thicknesses were investigated (0.3 and 0.8 mm), with their selection primarily based on previous research [12] and the associated likelihood of differing crack propagation behaviors (deflection versus penetration).

In the second approach, the specimen was printed with one half consisting of matrix material and the other half of IL material (Bi-layer configuration). The main objective of this approach was to identify potential differences in mechanical properties.

For the investigation of the H&H criterion, again two different types of specimens were printed (Fig. 2). To determine Π_{IL}, double-edge notched tension (DENT) specimens with fixed dimensions of $(110 \times 35 \times X (= 0.3 \text{ or } 0.8 \text{ mm}))$ mm³ were printed, while the theoretical ligament length, L_{th}, was varied between 5 and 15 mm (Sample c). To determine Π_i between the matrix and IL, DCB specimens (Sample d)

were fabricated with dimensions of $(62 \times 10 \times (20 + X (= 0.3 \text{ or } 0.8 \text{ mm})))$ mm³.

For the validation of both concepts, SENB specimens (Sample e) were printed, as illustrated in Fig. 2, with dimensions of $(55 \times 10 \times 10)$ mm³. As in the previous cases, two different IL thicknesses ($X = 0.3$ or 0.8 mm) were considered. In this case, however, the total specimen thickness was kept constant at 10 mm. Additionally, the distance from the machined notch to the first interface was consistently maintained at 0.4 mm (equivalent to four-layer heights in FFF), with the IL thickness varying away from the interface accordingly.

Within each test series, the specimens were printed sequentially, then removed from the build platform and stored under laboratory conditions (23 °C and 50 % r.h.) before testing.

2.3. Examination of the C&G approach by means of mechanical testing

For the validation of the C&G criterion, the determination of $\sigma_{m,IL}$, and σ_i is essential. The criterion suggests that cracks tend to deflect if the ratio of these two strengths ($\sigma_i/\sigma_{m,IL}$) is below 0.2. If the value exceeds 0.2, crack penetration is expected. While the criterion distinguishes between similar and dissimilar materials across the interface, a previous study [59] has shown that a mismatch in mechanical properties has minimal influence on the transition value of 0.2 - unlike the H&H criterion, where this fact plays a significant role.

2.3.1. Mono-material strength testing

The measurement of the mechanical properties of the mono-materials, including E_m, ν_m, and σ_m, was conducted using a Zwick Z010 universal testing machine from Zwick Roell (ZwickRoell GmbH & Co. KG, Germany). The determination of σ_m was performed on the previously mentioned 1BA test specimens. Force measurement was done using a 10 kN load cell (calibrated according to DIN EN ISO 7500-1 [60], class 0.5), while strain measurement was performed using digital image correlation (DIC) with the Mercury RT System (Sobriety s.r.o., Kuřim, Czech Republic). For this purpose, the specimens were coated with a fine speckle pattern, and deformation was tracked during testing using an Allied Vision Prosilica 6600 GT camera (Allied Vision Technologies, Germany) equipped with a Tokina AT-X 100 mm 2.8 Pro D lens (Keno Tokina Co., Ltd., Japan). Testing was performed following DIN EN ISO 527-2 [57]. The loading rate for the determination of E_m and ν_m was set to 1 mm/min. Thereafter, this rate was increased to 10 mm/min until specimen failure. Evaluation of E_m and ν_m was performed according to the mentioned standard within a strain range of 0.05 to 0.25 %. Clamping was achieved using 2.5 kN pneumatic grips, with a constant clamping length of 58 mm and a gauge length of 25 mm. In total, four specimens per material were tested under laboratory conditions (23 °C and 50 % r.h.).

2.3.2. Interface strength testing

For the measurement of σ_i, tensile specimens with dimensions of $(65 \times 10 \times 6)$ mm³ were used. Furthermore, two different approaches were employed for determining σ_I, as previously mentioned. In the first approach (Approach 1), the compliant IL was embedded between two matrix halves, with IL thicknesses of 0.3 and 0.8 mm. This method was chosen as it closely resembles the geometric conditions present in the final validation specimen. However, since this configuration results in two interfaces, failure could theoretically occur at either one, leading to variability within the specimen series. To mitigate this, a second approach (Approach 2) was introduced, where the compliant IL material was directly printed onto the matrix material, reducing the number of interfaces between dissimilar materials.

Regardless of the approach, all tests were conducted on a Zwick Z010 universal testing machine from Zwick Roell (ZwickRoell GmbH & Co. KG, Germany) following DIN EN ISO 527-2 [57]. The machine was equipped with a 10 kN load cell (calibrated according to DIN EN ISO 7500-1 [60], class 0.5). Local strain measurement was performed using a makroXtens extensometer (ZwickRoell GmbH & Co. KG, Germany) (calibrated according to DIN EN ISO 9513 [61], class 0.5) with a gauge length of 25 mm. The specimens were clamped using mechanical grips with a clamping length of 55 mm. The loading rate was set to 10 mm/min. The general test setup is illustrated in Fig. 3, exemplified for Approach 2. Three specimens per approach and IL thickness were tested under laboratory conditions (23 °C and 50 % r.h.).

2.4. Examination of the H&H approach by means of fracture mechanical testing

In contrast to the C&G criterion, the H&H criterion does not consider material strengths but rather fracture toughness values (Π_{IL}, Π_i). In cases where the materials surrounding the interface are identical (i.e., no mismatch in stiffness), the transition value between crack deflection and crack penetration is approx. 0.25 [25,32]. This value represents the ratio of G_d/G_p, where G_d is the energy release rate for a deflecting crack and G_p is the energy release rate for a penetrating crack.

However, if a mismatch in stiffness between the materials surrounding the interface is present, as is the case in this study, the transition value requires recalculation.

2.4.1. Determination of the transition value for crack deflection/crack penetration

As previously mentioned, the H&H approach for predicting failure modes is based on assumptions from LEFM. Strictly speaking, this approach should not be applied in the present case, primarily due to the use of the compliant IL material and the resulting high nonlinearity. Nevertheless, this concept will still be evaluated for its applicability in predicting failure modes and, of course, for comparison with the C&G criterion. The determination of G_d/G_p requires complex numerical integral equation methods, making it significantly more demanding compared to the C&G criterion. Additionally, numerous variables and parameters influence this calculation, as outlined in the study of Lee et al. [62] and the references listed there. For this reason, the G_d/G_p data used in this study were taken in their simplest possible form from the work of H&H [32] and applied to the analysis. These simplifications include assumptions such as incompressible material behavior and identical initial crack lengths for both crack deflection and crack penetration. More detailed insights into the determination of G_d/G_p and the factors influencing it can be found in previous studies [42,62,] and are beyond the scope of this work. Nonetheless, H&H [32] found in 1994 that the expression G_d/G_p primarily depends on the first Dundurs parameter [63], α. This parameter can essentially be interpreted as an elastic mismatch parameter between the matrix and IL material and is calculated as follows (Eq.1):

$$\alpha = \frac{\overline{E}_1 - \overline{E}_2}{\overline{E}_1 + \overline{E}_2} = \frac{E_{m,IL} - E_{m,Matrix}}{E_{m,IL} + E_{m,Matrix}} \tag{1}$$

where $\overline{E}_1$ represents the Young's modulus of the material after the first interface, the IL material, and $\overline{E}_2$ represents the Young's modulus of the matrix material. It should be noted that $\overline{E} = E_m$ corresponds to the tensile modulus in the case of a plane stress (PS) condition, and $\overline{E} = E_m(1 - \nu_m^2)$ corresponds to the tensile modulus in the case of plane strain (PE) [63]. Due to the small thickness of the tensile specimens, plane stress is assumed in this case, and $\overline{E} = E_m$ is applied. It should be noted that, for the sake of completeness, the case of PE was also considered in the results to evaluate its influence on the transition value, caused by a different stress state. However, for the final assessment of the H&H criterion, this transition value was not considered.

2.4.2. Mono-material fracture testing

To determine Π_{IL} of the compliant IL material, the essential work of fracture (EWF) method was used following ISO 2354:2022 [64]. The
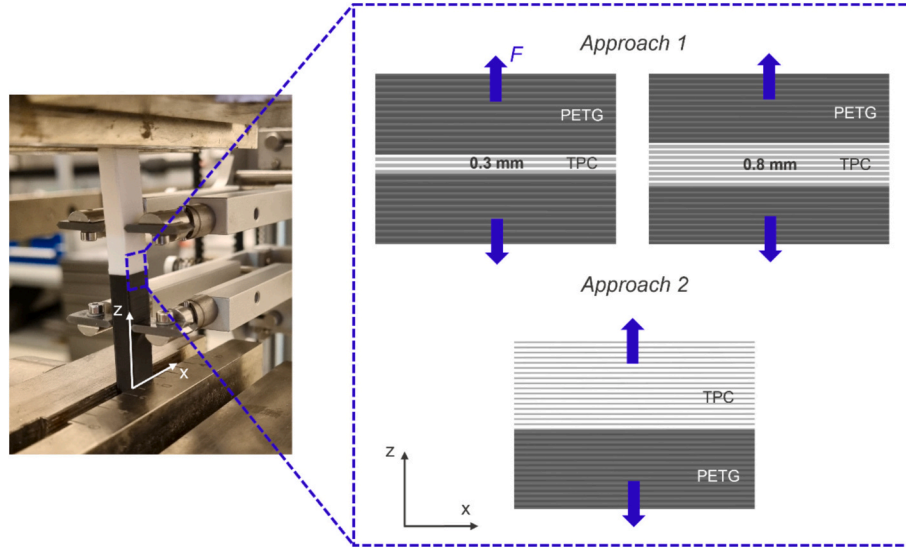
Fig. 3. Tensile test setup for determining the interface strength (σ_i) of the two investigated approaches (1 and 2); setup exemplarily shown for Approach 2.

choice of this methodology is primarily based on two key aspects that the compliant IL material exhibits. First, the IL material is a thermoplastic elastomer. The plastic zone that forms under mechanical loading is no longer small compared to the specimen dimensions, and thus the stress field at the crack tip can no longer be described by a stress intensity factor, such as that derived from LEFM. Secondly, the thickness of the soft IL is small. In reality, soft IL materials intended to act as crack stoppers are often thin polymer films rather than thicker components, which necessitates assuming a plane stress condition. The EWF method itself is based on the proposal by Broberg [65,66,] and has been further developed by other researchers [67], with a particular emphasis on those in the field of polymer science [68,69,]. When a cracked ductile material is subjected to stress, plastic deformation occurs in the so-called outer region or process zone. In this process zone, energy is mainly dissipated for the plastic deformation process. The outer region surrounds an inner region, the fracture process zone, where the actual crack process takes place, and energy is dissipated for chain breaks and disentanglements to create new surfaces. Based on these mechanisms, the overall fracture energy, W_f, can be divided into two main components, as shown in Eq. (2):

$$W_f = W_S + W_{pl} \tag{2}$$

where W_S, as previously mentioned, represents the energy necessary to create new surfaces. Therefore, assuming a proportional relationship to the fracture area ($L \cdot h$), the following expression results: $W_S = w_e \cdot h \cdot L$, where w_e represent the so-called essential work of fracture - EWF. For comparison, W_{pl} can also be expressed as $W_{pl} = w_p \cdot h \cdot L^2 \cdot \beta$ and is representative of the energy required for the plastic deformation of a certain volume in the process zone surrounding the fracture process zone. Here, w_p represents the so-called non-essential work of fracture - non-EWF, $h \cdot L^2$ is the volume, and β is a shape factor. When these relationships are considered in Eq. (2), it can be transformed into a specific fracture energy (energy per unit ligament area), w_{sf}, as shown in Eq. (3):

$$w_{sf} = w_e + \beta w_p L \tag{3}$$

To determine these parameters, w_e and $w_p \cdot \beta$, a series of samples with varying ligament lengths (L_{th}: 5, 6, 7, 8, 10, and 15 mm) and two different IL thicknesses (0.3 and 0.8 mm) were fabricated and subsequently tested. The introduction of sharp notches on both sides of the samples was carried out, regardless of the sample thickness, using metal templates. For this purpose, metal templates with different L_{th} values were cut using a laser. The unnotched printed DENT samples were then clamped between two templates, and sharp notches were manually introduced using a razor blade. It should be noted that the printed samples were made with an excess in length (0.5 mm on each side), and the final ligament length, L_{real}, was determined after the notching procedure. In all cases, the samples were notched in a way that met the standard's requirements [64] for the minimum (5 mm) and maximum (15 mm) L_{real}, with a given specimen width of 35 mm and a specimen length of 110 mm. Additionally, the maximum allowable crack tip radius of 10 μm, as prescribed by the standard [64], was verified using a digital light microscope (VHX-7000, Keyence Corporation, Japan) prior to testing.

The samples were tested on a universal testing machine, Zwick Z001 (ZwickRoell GmbH & Co. KG, Germany), equipped with a 1 kN load cell (calibrated according to DIN EN ISO 7500-1 [60], class 0.5). The same DIC system, camera, and lens as mentioned in Section 2.3.1 were used to measure the local deformation. Before the measurement, the samples were sprayed with a fine black pattern, as shown in Fig. 4. Deformation and the initial L_{real} were then determined using DIC, with a measurement length corresponding to the associated L_{real}, as specified in the standard [64]. The loading rate was set to 10 mm/min, as in the previous tests. The samples were clamped using pneumatic grips. In total, three samples for each IL thickness and L_{th} were measured under laboratory conditions (23 °C and 50 % r.h.). The recorded force-deformation curves were then used to calculate w_{sf} by integrating the curves and dividing by the cross-sectional area ($L_{real} \cdot h$). The data points were plotted in a w_{sf} vs. L_{real} diagram and subsequently fitted, taking into consideration the stress and the outlying data criterion [64] to determine w_e (intercept of the regression line with the ordinate) and $w_p \cdot \beta$ (slope of the regression line). Note that w_e are to be equated with Π_{IL} within this study.

2.4.3. Interface fracture testing

As highlighted in the introduction, a review of the current literature reveals that the determination of interface fracture toughness for combinations of stiff and compliant materials remains highly limited. In this study, a recently examined approach by Pakhare et al. [49] was adopted to determine Π_i. This method is based on a stiffness drop technique and uses a finite element model of the experiment to evaluate fracture toughness using J-integral [70]. Essentially, the current study followed the procedure of the aforementioned work, applying it to the PETG & TPC interface to determine Π_i. The multi-material DCB specimens were printed using the specified parameters. Initially, the matrix material was printed, and the material change to TPC was leveraged to place a thin Kapton film (approx. 25 mm in length) at the first PETG to TPC interface
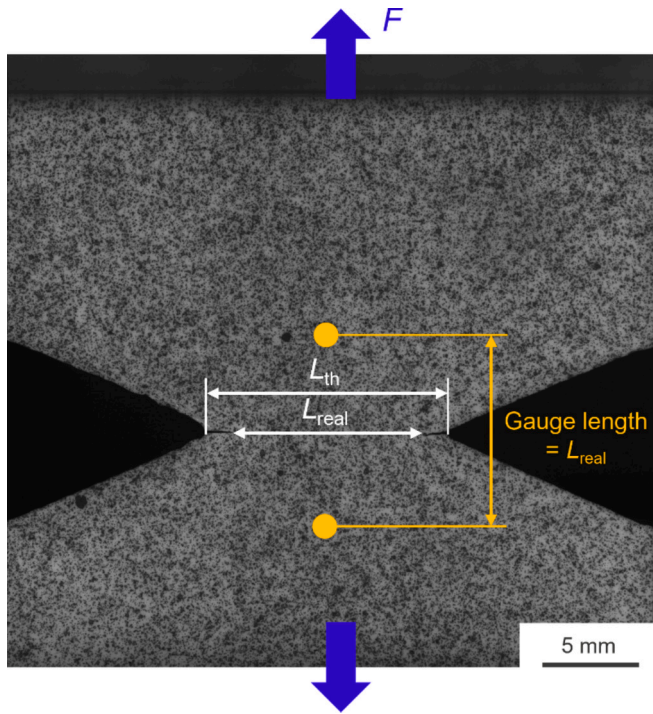
Fig. 4. Setup for the determination of the fracture toughness of the compliant interlayer (Π_{IL}) using the essential work of fracture (EWF) approach on a double-edge notched tension (DENT) specimen; L_{th} represents the theoretical, while L_{real} denotes the real ligament length.

to act as a pre-crack. This resulted in an initial crack length, a_0, of approx. 20 mm, as illustrated in Fig. 5. The exact a_0 value was subsequently measured after the fracture experiments using a digital light microscope (VHX-7000, Keyence Corporation, Japan). Following this, the compliant IL material was printed over the Kapton film. The final specimen dimensions were (62 × 10 × 20.3) mm³ for an IL thickness of 0.3 mm and (62 × 10 × 20.8) mm³ for an IL thickness of 0.8 mm. Prior to testing, the initial crack region was carefully cleared using a 1 mm thick saw blade, extending up to 5 mm ahead of the sharp crack tip to facilitate unrestricted opening of the crack flanks (Fig. 5). The specimens were fixed in a designated fixture using metal pins (4 mm in diameter) and subsequently subjected to Mode I loading at a constant loading rate of 10 mm/min.

Testing was conducted using a Zwick Z010 universal testing machine (ZwickRoell GmbH & Co. KG, Germany) equipped with a 10 kN load cell (calibrated according to DIN EN ISO 7500-1 [60], class 0.5). Deformation measurements were recorded using the previously mentioned DIC system under the same setup. The DIC was also employed to estimate crack initiation, although precise visual identification was significantly limited due to high nonlinearity and crack tip blunting. Therefore, the 15 % stiffness drop method, as described in Ref. [49], was applied to determine the critical crack initiation force, F_c. This loading condition was subsequently used in a 2D plane strain finite element model where Π_i was evaluated. This was done by computing the *J*-integral along a contour path surrounding the crack front, using the native implementation available in ABAQUS (Dassault Systèmes, France). The PETG was modeled as a linear elastic material, while the TPC behavior was defined using the Arruda-Boyce hyperelastic law, calibrated from uniaxial tensile test data. Both materials were assumed isotropic, which is a reasonable assumption given that the deformation is dominated by in-plane bending [46,49,71].

A detailed explanation of the stiffness drop method and the finite element analysis is beyond the scope of this study, but can be explicitly found in the work of Pakhare et al. [49]. Any modifications to their approach, if applicable, have already been specified. In total, three specimens per IL thickness were tested under laboratory conditions (23 °C and 50 % r.h.).

2.5. Multi-material fracture testing and accuracy of failure mode prediction

To assess the applicability of the C&G and H&H criteria for crack deflection/penetration prediction in multi-material FFF printed structures, SENB specimens with dimensions of (55 × 10 × 10) mm³ were fabricated. For validation, two IL thicknesses, 0.3 and 0.8 mm, were investigated. It is important to note that the incorporation of the IL layers was designed in such a way that it did not increase the overall height of the specimens; instead, the stiff matrix ligament was modified after the second interface (transition from TPC to PETG). As shown in Fig. 6, the machine notch was considered during the printing of the specimens, which provided the advantage of a narrow gap. This narrow gap defined the position for the sharp crack introduction. A sharp razor blade was attached to a microtome (Leica RM2255, Leica Microsystems GmbH, Austria) for crack introduction. The crack was then introduced by a smooth up-and-down movement of the blade (broaching). Additionally, the way the specimens were printed ensured that, from the machine notch to the first PETG/TPC interface, regardless of the IL thickness, the same number of printed layers was maintained. This spacing was kept constant at 0.4 mm (4 printed layers) across all specimens, providing the advantage of precisely positioning the sharp notch close to the interface, as detailed and discussed in a previous study [21].
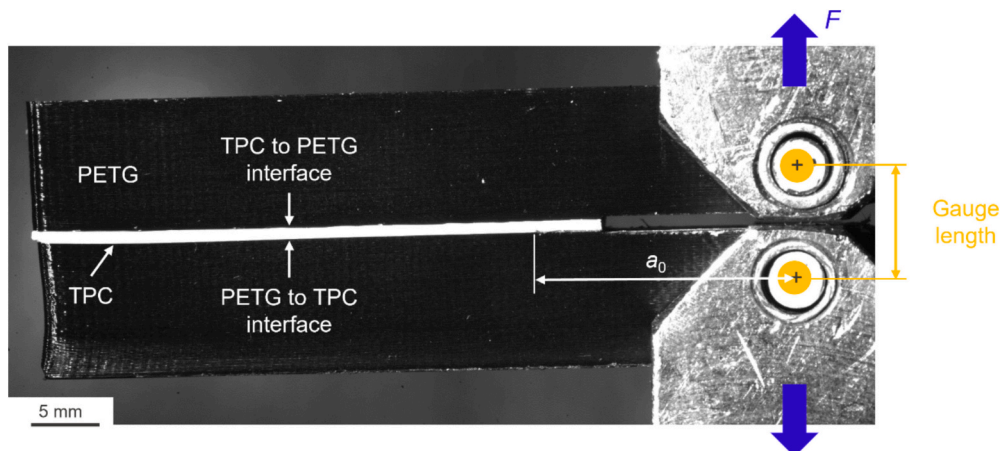
Fig. 5. Test setup for the determination of the interface fracture toughness, Π_i, between the selected materials PETG and TPC; a_0 represents the initial crack length.
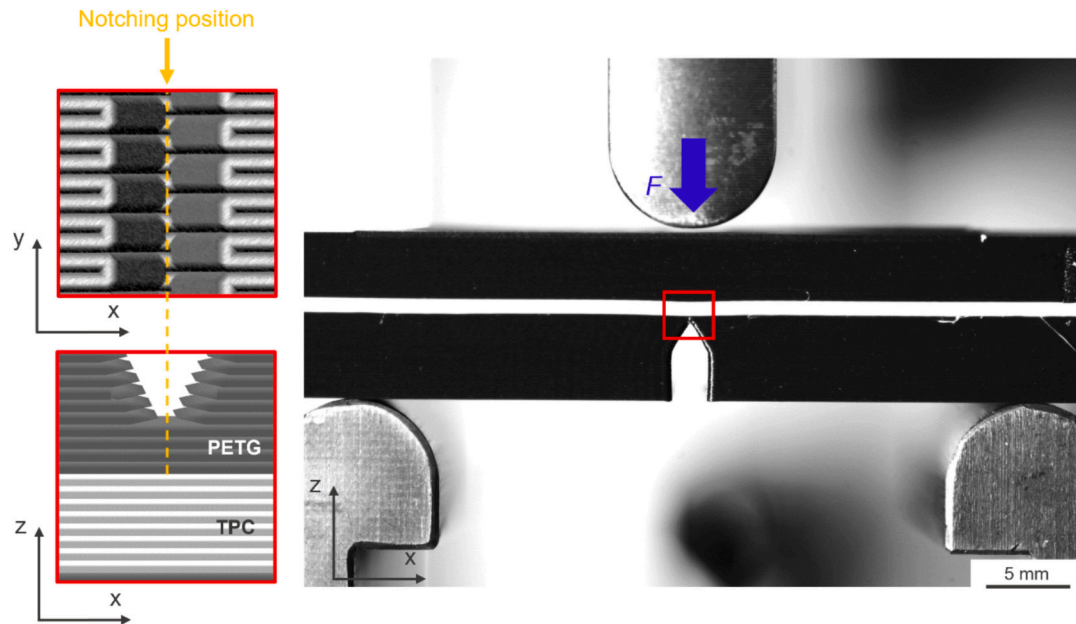
Fig. 6. Experimental setup used for the validation of the criteria through single-edge notched bending (SENB) specimens with a detailed view of the notch position.

The exact positioning of the crack tip is particularly crucial for the validation of the H&H criterion, which, as mentioned, assumes a crack positioned at an interface, in contrast to the C&G criterion. Moreover, positioning the crack tip close to the interface offers the advantage of eliminating dynamic effects that may occur during crack propagation. However, in all cases, the initial crack length and the remaining specimen geometries were selected to meet the requirements stated in the standard [72], with $0.45 < a_0/W < 0.55$, where W (=10 mm) represents the specimen width.

Force and displacement measurements were conducted using a Zwick Z010 universal testing machine (ZwickRoell GmbH & Co. KG, Germany), with the testing procedure aligned with ASTM D5045 [72]. The force was measured using a 10 kN load cell (calibrated according to DIN EN ISO 7500-1 [60], class 0.5), and the local displacement was recorded using a macroXtens extensometer (ZwickRoell GmbH & Co. KG, Germany; calibrated according to DIN EN ISO 9513 [61], class 0.5). A 5 mm radius was chosen for the supports and fin. The support distance was maintained at 40 mm, as specified in the standard (4·W) [72]. The loading rate was set to 10 mm/min to maintain consistency with the other experiments. In total, three tests were performed for each IL thickness under laboratory conditions (23 °C and 50 % r.h.).

The experiments conducted are solely intended to validate the concepts. A calculation of the fracture toughness of multi-material FFF SENB specimens has been deliberately omitted in this case. The primary reason for this decision is the difficulty of obtaining a correct and acceptable evaluation. Strictly speaking, existing standards are only applicable to macroscopically homogeneous materials, and inhomogeneities, such as the compliant IL sandwiched between the stiff matrix, are not considered. Furthermore, to validate the mentioned criteria, evaluating this data is not necessary. Therefore, the discussion of the results in this case will be limited to a detailed analysis of the force-displacement curves and an examination, according to the standard [72], of the nonlinearities as well as the size of the plastic zone, to draw conclusions about the prevailing stress state.

For crack progression detection (deflection or penetration), the previously mentioned DIC system was employed with the unchanged setup, as described above. It is important to note that only the direction of crack growth at the initiation stage is of interest. Since both criteria are based on LEFM, further crack progression is generally not of concern.

According to the C&G criterion, cracks should deflect if the ratio of

$\sigma_i/\sigma_{m,IL} < 0.2$; otherwise, crack penetration through the compliant IL is expected. According to the H&H criterion, crack deflection is expected if the new recalculated ratio of $G_d/G_p \geq \Pi_i/\Pi_{IL}$. Otherwise, crack penetration is anticipated. Moreover, it should be noted that the transition models proposed by C&G and H&H are based on Mode I loading. In this study, Mode I tensile specimens were likewise used to determine the required bulk and interface properties. However, validation was performed using a bending test specimen, which introduces a slightly different crack tip loading condition (Mode I/Mode II). While this deviation is not expected to significantly influence the results, it is mentioned here for the sake of completeness.

However, to ensure the significance of the validation tests and the predictions made by the criteria, it was stipulated that all three validation tests must exhibit the same failure mechanism within a given IL thickness. If this is not the case, the results will be considered inconclusive.

3. Results and discussion

Before presenting and discussing the results regarding the suitability of the two investigated criteria for predicting the failure mode, all findings related to the mono-material and interface properties will be presented and analyzed in detail.

3.1. Examination of the C&G approach by means of mechanical testing

3.1.1. Mono-material strength testing

Fig. 7 presents the stress-strain diagrams of the two mono-materials, Matrix and IL, with one representative curve per material out of four sample runs (n = 4). In this respect, Table 1 summarizes the key mechanical properties relevant to this study, such as E_m, ν_m, and σ_m.

The stress-strain diagrams indicate that the two mono-materials exhibit different deformation behaviors under tensile loading in the x-direction. The matrix material has a higher E_m and σ_m than the IL material. Additionally, a yield point followed by a cold drawing region and a slight onset of strain hardening is observed. The elongation at break is lower in comparison to the IL material.

The deformation behavior of the IL material corresponds to that of a typical thermoplastic elastomer [73], characterized by an initial linear behavior with a low E_m, followed by a pronounced nonlinear
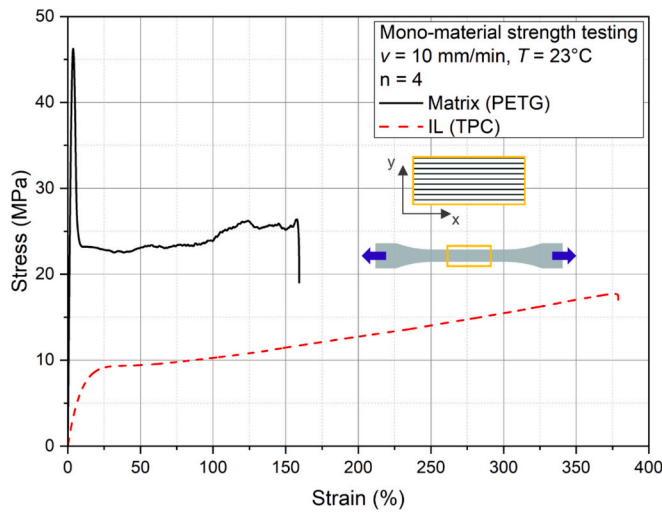
Fig. 7. Representative stress-strain diagram for the matrix (PETG) and IL (TPC) mono-materials.

Table 1
Results of the mono-material strength testing.

	E_m (MPa)	ν_m (−)	σ_m (MPa)
Matrix	2076 ± 81	0.42 ± 0.01	47.0 ± 0.5
IL	97 ± 6	0.49 ± 0.01	17.7 ± 0.4

hyperelastic behavior. Due to the elastomeric components within the TPC, the elongation at break is higher than that of the matrix material, whereas σ_m is lower.

E_m values are 2076 ± 81 MPa and 97 ± 6 MPa for the matrix and IL material, respectively. Compared to the values reported in the manufacturer's datasheets (Section 2.1), the measured values for the IL material show good agreement. However, the data for PETG exhibit a significant deviation of approx. 600 MPa. This discrepancy can primarily be attributed to differences in printing parameters. While the presented data were obtained using the printing parameters presented in Section 2.2, the samples referenced in the datasheet [54] were printed with higher layer heights (0.2 mm) and printing speed (200 mm/s). Both parameters generally influence E_m.

It is well known that a lower layer height increases mechanical properties such as E_m and σ_m. This can be explained, e.g., by the reduced distance between the nozzle and the previously deposited strand. The shorter distance leads to higher pressure between the newly deposited and the pre-existing strand during printing. Additionally, this shorter distance promotes re-melting of the previously deposited strand, which enhances wetting, neck formation, and diffusion processes between individual strands and layers [74]. Another advantage of lower layer heights, which contributes to improved mechanical properties, is the increased melt flow rate when all other printing parameters remain constant. This can reduce void formation between individual layers and strands [75,76]. Similarly, printing speed can significantly affect mechanical properties. Higher printing speeds reduce the time available for adequate wetting, neck formation, and diffusion processes, which results in weaker interfacial bonding between individual strands and layers. The critical factor for this formation of interfacial bonding is the time the material remains above its glass transition temperature during strand deposition [20]. As demonstrated by Wang et al. [77], printing speed also has a strong influence on the macrostructure. Parts printed at higher speeds tend to exhibit larger voids, which has a detrimental effect on interfacial bonding.

However, the measured E_m value for the IL material falls within the range specified in the manufacturer's datasheet [55]. Due to the

difference in the matrix material, the resulting E_m ratio is approx. 21, compared to the previously mentioned theoretical ratio of around 16 (Section 2.1). Furthermore, ν_m is 0.42 ± 0.01 and 0.49 ± 0.01 for the matrix and IL material, respectively. The σ_m values are 47.0 ± 0.5 MPa for the matrix material and 17.7 ± 0.4 MPa for the IL material. These values are specifically critical for assessing the predictive capability of the failure mode according to the C&G criterion.

3.1.2. Interface strength testing

Fig. 8 presents the results of the investigation into interface strength. In Fig. 8A, a representative (n = 3) stress-strain diagram for each Approach (1 and 2) is shown, along with a corresponding fracture surface. Fig. 8B presents a comparison of the σ_i values, with the corresponding data provided in Table 2.

Fig. 8A and Fig. 8B, as well as Table 2, indicate significant differences in σ_i, depending on the approach used. The fracture images in Fig. 8A reveal that in Approach 1, the fracture only partially occurred at the interface, whereas the fracture pattern of the bi-layer configuration appears more uniform, indicating that failure predominantly occurred at the interface. For this reason, the value of 6.7 ± 0.3 MPa from the bi-layer configuration is used in the subsequent evaluation of the C&G criterion to assess its suitability for predicting the failure mode.

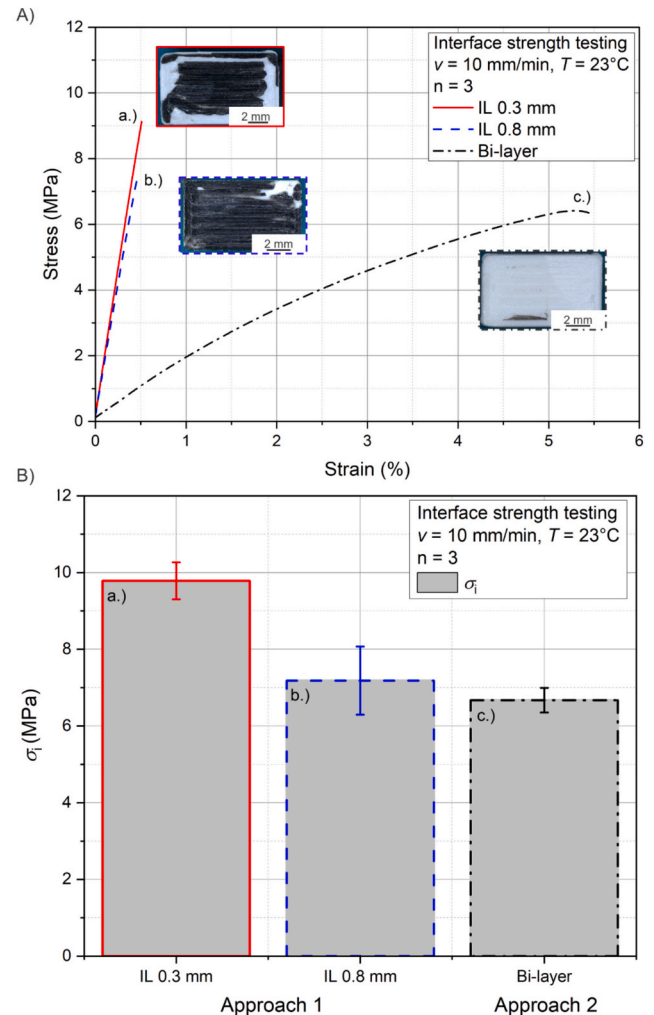Nevertheless, the question remains as to why the failure behavior

Fig. 8. Representative stress-strain diagram for the investigated Approaches 1 (IL 0.3 and 0.8 mm) and 2 (bi-layer) with corresponding fracture surfaces (A); comparison of the different Approaches 1 and 2 concerning interface strength, σ_i, of the different sample configurations used (B).

Table 2
Results of the interface strength testing.

|	σ_i (MPa)
IL 0.3 mm	9.8 ± 0.5
IL 0.8 mm	7.2 ± 0.9
Bi-layer	6.7 ± 0.3

differs both visually and numerically. A possible explanation may lie in the printing approach used, in combination with the selected materials and sample configurations.

In Approach 1, the sample features a symmetrical design with two interfaces present (PETG to TPC – lower interface and TPC to PETG – upper interface, with respect to print direction and tensile direction), whereas in the bi-layer configuration (Approach 2), only a single interface (PETG to TPC) is present. When considering the viscosity differences of both materials at the applied printing temperature of 240 °C (Appendix A), variations in mechanical properties arise depending on which interface is examined. The IL material exhibits a roughly eight times higher melt flow rate (MFR) and thus a lower viscosity compared to the matrix material, which suggests that bonding is enhanced at this lower interface due to improved wetting and neck formation. Consequently, in Approach 1, failure does not occur at the lower interface but rather at the upper one. In contrary, the sample in Approach 2 offers only one significant weak point, the interface between PETG and TPC.

The slightly higher σ_i values obtained in Approach 1 can be attributed to a mixed or out-of-plane failure between the IL and matrix material, which is not present in the bi-layer configuration. This mixed failure mode in Approach 1 could be linked to the operational characteristics of the 3D printer used. The printer functions by alternating filament extrusion rather than employing multiple print heads for multi-material printing. This setup not only extends the overall print time but also introduces the disadvantage of cooling between material changes, which can negatively impact the mechanical properties. Additionally,

this printing method requires the use of a purge tower to remove residual material from the nozzle during a material change. If this cleaning process is insufficient, the interface may not have a clear separation between the two materials, resulting in smearing or intermixing. Another aspect that must be considered is the fact that PETG, a material with a higher melting point and viscosity, is deposited onto a material with a lower melting point and significantly lower viscosity. This can result in further smearing of the TPC layers during PETG strand deposition. These effects resulting from the printing process are illustrated in Fig. 9. While the PETG to TPC interface shows a distinct separation of the materials (Detail A), the TPC to PETG interface appears irregular and smeared (Detail B). Such smearing can lead to a mixed failure mode, as observed in this study. On the one hand, higher forces are required to break the specimen, as failure occurs not only between two distinct printed layers but across multiple layers, including the breaking of strands in the z-direction. On the other hand, however, this intermixed region exhibits numerous irregularities and defects, which may lead to premature and unreliable failure under mechanical loading. From a testing perspective, the approach used in Approach 2 is preferable to Approach 1, as the primary objective is to determine the interface strength. This methodology or approach is also the one that is commonly used in the literature [45,78].

However, the stress-strain responses of the interface strength tests shown in Fig. 8A differ significantly from those of the mono-material strength test in Fig. 7. This discrepancy is primarily attributed to the orientation of individual strands and the load application within the tensile test. In the mono-material test, the load is applied along the strand deposition direction (x-direction), allowing the filaments to bear the forces, thereby making the bonding strength between individual strands and layers less significant. In contrast, during the interface strength tests, the load must be carried by the interfaces and their respective bonding strengths (z-direction), which often leads to more brittle failure, as demonstrated in various studies [27,79,80].
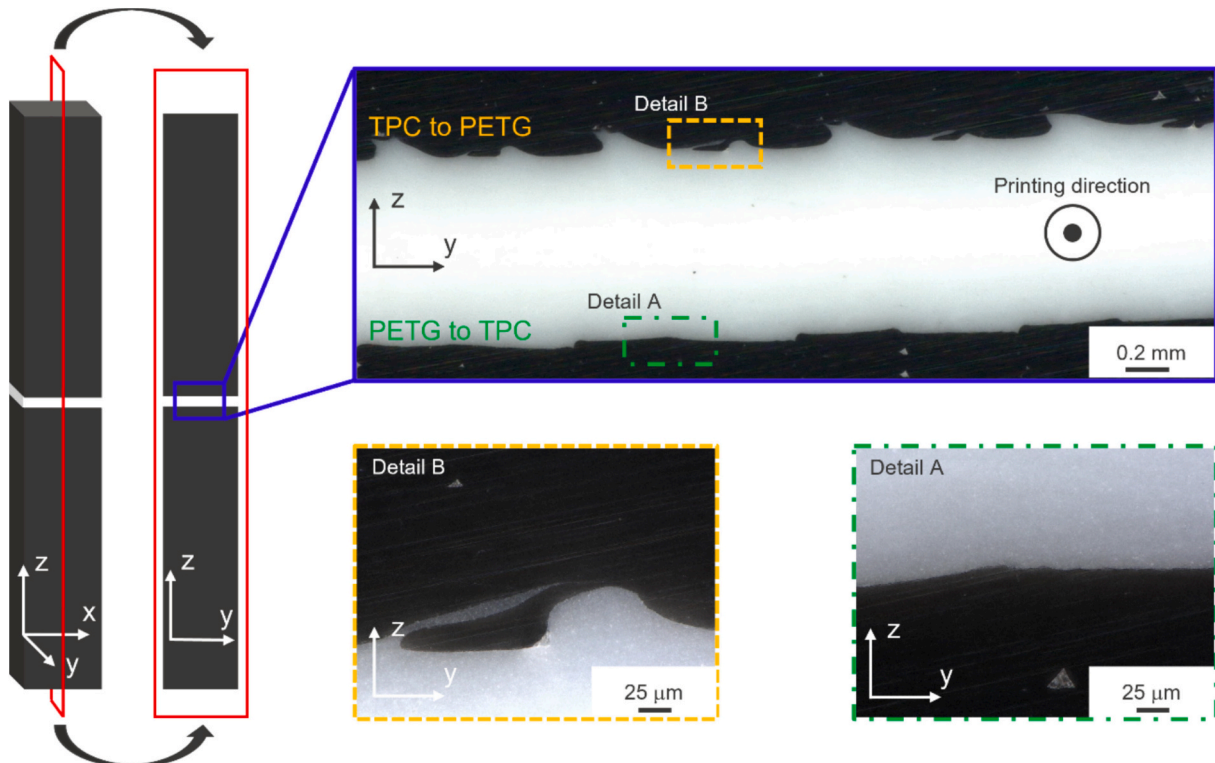
Fig. 9. Overview of the interfaces generated by the printing process used in Approach 1 for an IL thickness of 0.8 mm.

3.2. Examination of the H&H approach by means of fracture mechanical testing

3.2.1. Determination of the transition value for crack deflection/crack penetration

Fig. 10 presents G_d/G_p as a function of α for single-sided (solid black line) and double-sided (blue dashed line) crack deflection. Additionally, the respective regions indicating whether crack deflection or crack penetration is expected, according to the H&H criterion, are marked.

Table 3 summarizes the results in terms of the recalculated transition values for the PS and PE conditions, differentiating between single- and double-deflecting cracks.

The data indicate that the calculated α value, in the case of PS conditions, of -0.91 ± 0.05 is already at the boundary of the H&H plot, which can be attributed to the significant mismatch in E_m of the investigated materials. Therefore, the last calculated values from the plot were used (-0.9), which should have only a minimal impact on the final predictions. For single crack deflection, the transition value to crack penetration is approx. 0.55, while for double crack deflection, it is around 0.38. Consequently, if single crack deflection occurs in the validation specimens, the ratio Π_i/Π_{IL} should fall between 0.38 and 0.55, according to the criterion. If the ratio exceeds this range, crack penetration is expected in the validation specimens, whereas a lower ratio suggests double crack deflection.

For the sake of completeness, Table 3 also includes the values for the PE condition, which are provided for comparison purposes only. These values are not considered in the subsequent evaluation of the H&H criterion, as the specimen thickness suggests a plane stress condition rather than a plane strain condition. The calculated α value in this case is -0.92 ± 0.07. Consequently, the α values do not exhibit a significant difference depending on the stress state.

3.2.2. Mono-material fracture testing

Fig. 11 presents the force-displacement curves of the compliant IL material obtained from the EWF investigations, with one representative curve plotted per IL thickness and L_{th} out of three sample runs (n = 3). Additionally, specific markers (P1 to P5 for a specimen thickness of 0.3 mm and D1 to D5 for a specimen thickness of 0.8 mm) are highlighted on the force-displacement curve for $L_{th} = 15$ mm. These markers illustrate the crack propagation within the compliant DENT specimen as displacement increases.

Table 3
Overview of the calculated transition values from the H&H plot.

| Required mechanical properties from mono-material strength testing		
	IL	Matrix
E_m (MPa)	97 ± 6	2076 ± 81
ν_m (−)	0.49 ± 0.01	0.42 ± 0.01
Calculated Dundurs parameter for different stress states		
Stress state	PS	PE
α (−)	-0.91 ± 0.05	-0.92 ± 0.07
Calculated transition values for different stress states		
G_d/G_p (−)	Single crack deflection	Double crack deflection
PS	0.55	0.38
PE	0.55	0.38

The force-displacement curves indicate that the force level required for plastic deformation in the process zone and crack propagation in the fracture zone is approx. Three times higher for a specimen thickness of 0.8 mm compared to 0.3 mm. Furthermore, independent of the thickness, the curves exhibit self-similarity with varying L_{th}, which is a requirement for result validity as outlined in Ref. [64]. It is also evident that the printed specimens used in this study cannot be directly compared to homogeneous bulk materials and their characteristic curves, as shown, e.g., in Ref. [81]. This is due to inherent process-related variations in FFF, which inevitably influence the micro- and macrostructure of the specimens. In particular, the orientation of the strands relative to the initial, along with the resulting microstructure, plays a crucial role in the fracture behavior of FFF specimens. This has been demonstrated in studies by, e.g., Verma et al. [82] on ABS and Lorenzo-Bañuelos et al. [83] on polypropylene (PP) specimens. In the latter, variations in failure modes were observed in 0°-oriented PP samples, with particular emphasis on fluctuations in the printing process as a contributing factor. Similarly, Zhang et al. [84] reported comparable findings in polyether-ether-ketone (PEEK), highlighting the significance of crack tip positioning in 0°-oriented samples. Their research indicates that the crack tip position at an interface can influence fracture behavior and introduce scatter in the results. However, a separation of adjacent strands as described in these studies did not occur visibly in the investigations on TPC samples used in this study, which can partly be attributed to the low porosity (~1 %) of the printed samples (Appendix A.2).

Another requirement for obtaining valid results using the EWF
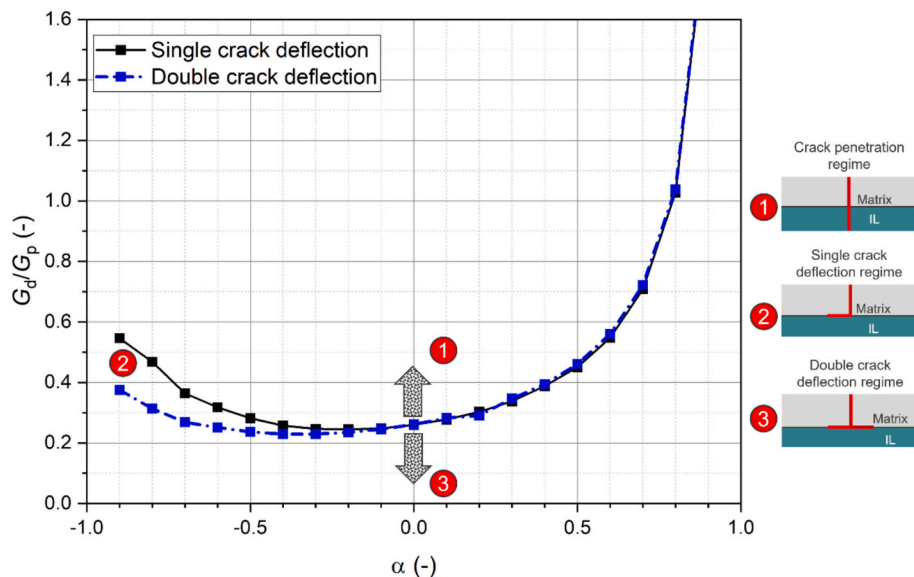
Fig. 10. H&H plot for the determination of the transition values between crack deflection and penetration under the assumption of tensile load. Ratio of the energy release rate for a deflecting and penetrating crack, G_d/G_p, as a function of the first Dundurs parameter, α.
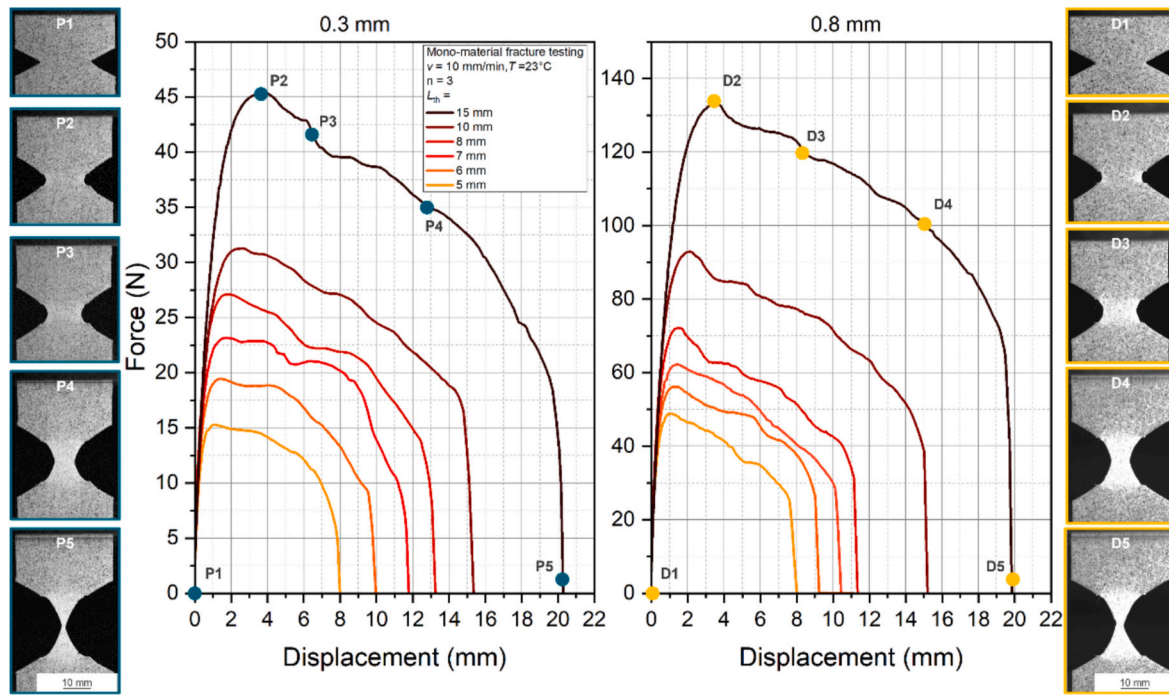
Fig. 11. Force-displacement curves for different theoretical ligament lengths (L_{th}) of the mono-material fracture tests shown for the two specimen thicknesses investigated (0.3 and 0.8 mm). The points P1-P5 and D1-D5 indicate fracture and plastic zone formation with increasing sample deformation.

method is that the unnotched ligament must yield before crack onset occurs [64]. This requirement ensures that the fracture mechanism remains consistent regardless of L_{th}. In the investigated material, identifying such yielding prior to crack onset is challenging due to the material's white pigmentation. At positions P2 and D2 (corresponding to the force maxima of the curves), the formation of a plastic zone is already apparent. However, complete yielding of the ligament is only observed at P3 and D3. Notably, this is also the point at which the first crack propagation is detected. This suggests that, for the examined material, full plasticization of the unnotched ligament and crack onset occur almost simultaneously. A similar behavior was also observed, e.g., by Rink et al. [81] in thin PETG films.

Fig. 12 presents w_{sf} as a function of L_{real} for the two different specimen thicknesses, 0.3 and 0.8 mm. The results of the investigation are summarized in Table 4. The findings indicate that Π_{IL} does not exhibit a
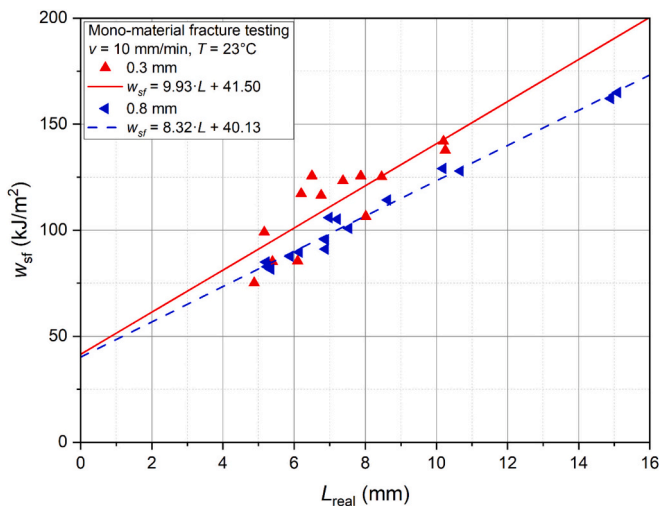
Table 4
Results of the mono-material fracture testing.

Specimen thickness (mm)	Π_{IL} (kJ/m^2)	$\beta \cdot w_p$ (MJ/m^3)	r^2
0.3	41.50 ± 14.80	9.93 ± 2.01	0.6893
0.8	40.13 ± 2.69	8.32 ± 0.31	0.9826

statistically significant difference within a 95 % confidence interval, regardless of specimen thickness. The values of 41.50 ± 14.80 kJ/m^2 and 40.13 ± 2.69 kJ/m^2 for IL thicknesses of 0.3 and 0.8 mm, respectively, fall within a similar range. However, a notably higher scatter in Π_{IL} is observed for the 0.3 mm specimen thickness, which is confirmed by the lower coefficient of determination (r^2 = 0.6893). Additionally, the slope of the regression line ($\beta \cdot w_p$) is slightly higher, although not statistically significant. This increased variation in values may be attributed to geometric constraints associated with thinner specimens. Furthermore, process-induced fluctuations during printing cannot be ruled out, as such variations tend to have a more pronounced effect on measurement results in thinner specimens than in thicker ones. Small defects in thinner samples can have a greater impact on fracture testing outcomes than their effect in thicker specimens. To give an example, Maspoch et al. [85] demonstrated in poly(ethylene terephthalate) (PET) bulk films that thickness generally influences the slope of the regression line rather than Π_{IL}.

To assess the plausibility of the obtained values for TPC, relevant studies mentioned in this section were reviewed and used as reference points. Verma et al. [82] reported a fracture toughness value of 6.9 ± 1.38 kJ/m^2 for 1 mm thick ABS samples printed with 0°-orientation. Lorenzo-Bañuelos et al. [83] measured approx. 35.1 kJ/m^2 in 0.5 mm thick, 0°-oriented printed PP samples. Sharma et al. [86] determined a fracture toughness of 32.1 kJ/m^2 in 0.5 mm thick, 0°-oriented PEEK specimens. Similarly, Zhang et al. [84] applied the EWF approach to 0.5 mm thick, 0°-oriented PEEK samples and obtained a value of 12.17 ± 0.50 kJ/m^2. The variations in fracture toughness between these two PEEK studies may be attributed to differences in the PEEK manufacturer, the 3D-printer used, and specific printing parameters. Additional

Fig. 12. Specific fracture energy (w_{sf}) as a function of the real ligament length (L_{real}) for the two investigated TPC thicknesses, 0.3 and 0.8 mm.

fracture toughness values for polymer bulk materials, which are not directly related to FFF, can be found in [87]. Notably, the fracture toughness of materials such as linear low-density polyethylene (LLDPE) or ethylene-(vinyl acetate) copolymer (EVOH) falls within the same range as the TPC values determined in this study. Moreover, the values are also in close agreement with those reported by Lee et al. [88], who investigated various commercially available thermoplastic elastomers. Depending on the material type, the degree of molecular orientation resulting from the injection molding process, and the orientation of the initial crack relative to this alignment, they reported values ranging from around 34 to 71 kJ/m^2.

3.2.3. Interface fracture testing

Fig. 13 presents the force-deformation curves, with one representative curve for each IL thickness (0.3 and 0.8 mm) out of three sample runs (n = 3). From the diagram, it is evident that regardless of the IL thickness, the curves initially exhibit a linear increase. This initial increase is interrupted at around 0.2 to 0.3 mm of deformation by a discontinuity, which can be attributed to the detachment of the remaining Kapton film, which served as the initial pre-crack. Following this, the curves continue to increase linearly until F_c (Marker 1) is reached, indicating the point of crack initiation. Around this critical force, the curve starts to deviate from linear behavior, reaches a maximum force (F_{max}; Marker 3), and thereafter decreases. Marker 2 in the force-deformation curves represents the force value at which the first crack propagation was detected by DIC ($F_{c, optical}$). Consequently, at around F_c, crack blunting occurs along with the first signs of damage in the process zone surrounding the crack tip. The small area between F_c and $F_{c, optical}$ marks the onset of crack growth. Interestingly, the initial portions of the curves are identical, suggesting that differences in IL thickness do not significantly influence stiffness at this stage. However, substantial differences in the curve progression beyond F_c and $F_{c, optical}$ indicate variations in crack blunting and subsequent crack propagation. These findings align well with the results reported by Pakhare et al. [49] in their studies on ABS/TPU/ABS DCB specimens.

One notable discrepancy, not addressed in their study and for which no supporting evidence is stated, is the delamination of the matrix material from the IL material at the second, non-cracked interface (TPC to PETG), which was consistently observed at F_{max} across all specimens. The underlying causes for this phenomenon are manifold and, as previously discussed in the interface strength analysis, are likely attributable to the chosen printing technique in combination with viscosity differences between the materials. Fig. 14 shows the fracture surface of PETG to TPC, as well as the partially detached TPC to PETG interface of

the specimens for IL 0.8 mm. The PETG to TPC interface appears relatively smooth, with no visible TPC residues, reflecting a clean deposition of the TPC strands onto the PETG layer during the printing process. In contrast, the TPC to PETG interface exhibits TPC residues, which, as already discussed in Section 3.1.2 (Fig. 9), can be attributed to intermixing of the two materials during the printing process. However, this experiment reveals a difference in the interfacial bond strength of the two interfaces, similar to the results previously presented in Section 3.1.2. Despite the intermixing of both materials, the TPC to PETG interface appears to exhibit lower bond strength than the PETG to TPC interface. This suggests that such intermixing tends to generate irregularities and, consequently, defects rather than improving the bond strength among the selected materials and printing technique. In general, however, it has been observed that bond strength increases with greater contact area [45,89,90], and that material intermixing at interfaces can, in some cases, have a positive effect on interfacial bond strength [91].

Nonetheless, this occurrence is not expected to affect the overall findings, as crack initiation occurs before reaching F_{max} in both cases. Further crack growth is not of primary relevance to the scope of this study. However, with a focus on crack initiation, it should be noted that this phenomenon strongly depends on the selected material pairing as well as on the chosen printing parameters, which in turn determine the size and shape of defects and voids within a printed structure [92]. In this study, the porosity of the individual printed structures is generally very low, amounting to 4.0 ± 0.5 % for PETG and 1.0 ± 0.1 % for TPC (Appendix A.2), which can be attributed primarily to the printing parameters used. This naturally affects both interlayer and intralayer bonding strength, and consequently, the fracture toughness of interfaces within a single material as well as between dissimilar materials, since the size and morphology of voids can induce varying stress concentrations [93]. In the present case, the interface involves dissimilar materials. Due to the low viscosity of TPC, it can easily flow between the deposited PETG strands, thereby promoting good wetting. Upon crack initiation and subsequent crack propagation, the two materials must be separated, which requires a certain amount of force that may also vary depending on the material combination and printing parameters, as demonstrated, e.g., by Altuntas et al. [94] for PLA/TPU.

Table 5 presents the results of the interface fracture tests. The data, as well as Fig. 13, indicate that F_c increases with increasing IL thickness, rising from 74.1 ± 3.4 N for 0.3 mm to 88.1 ± 5.2 N for 0.8 mm. This trend is largely consistent with observations reported in the literature [95]. The values of Π_i differ significantly (95 % confidence interval). Specifically, Π_i for an IL thickness of 0.3 mm is 0.37 ± 0.04 kJ/m^2, whereas for 0.8 mm, it is 0.61 ± 0.01 kJ/m^2, corresponding to an increase of approx. 65 %, highlighting the dependence of Π_i on IL thickness on a macroscopical scale. This increase can primarily be attributed to the enlargement of the process zone around the crack tip, which enhances energy dissipation. However, it is important to note that Π_i cannot increase indefinitely with the IL thickness. As demonstrated in Ref. [49, 96], an optimal IL thickness may exist, beyond which Π_i may begin to decrease with further thickness increases.

Despite this, Π_i between PETG and TPC remains relatively low compared to Π_{IL} of pure TPC. Although both materials share a similar chemical base, differences in, e.g., morphology (amorphous vs. semi-crystalline) can lead to limited compatibility, which is reflected in the low Π_i values. Furthermore, it should be noted that the crack tip radius, influenced by the thickness of the film, is slightly larger than that typically observed using traditional crack introduction methods [97], potentially affecting Π_i values and limiting direct comparability with literature data. Nevertheless, compared to other MMAM material combinations, the values obtained in this study seem plausible. For instance, Π_i for PLA/TPU is approx. 0.048 ± 0.01 kJ/m^2 [46], for PLA/Nylon it varies between 0.036 and 0.135 kJ/m^2, depending on printing temperature, build platform temperature, printing speed, layer height, and orientation [47]. Additionally, ABS/TPU, depending on the thickness of
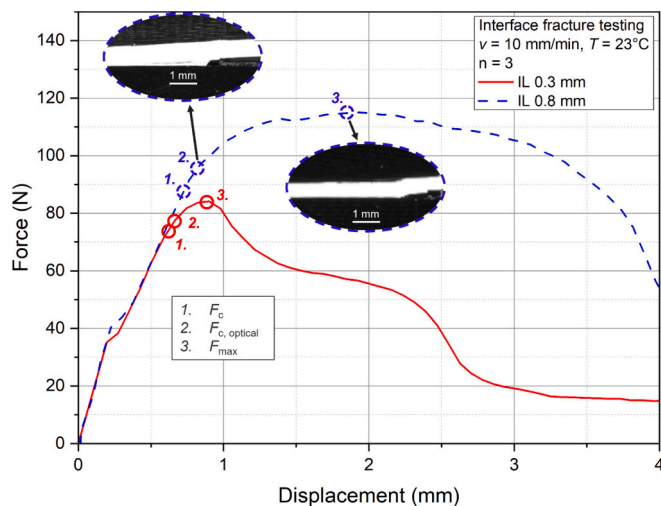

Fig. 13. Force-displacement curves from interface fracture testing for the two investigated IL thicknesses (0.3 and 0.8 mm).
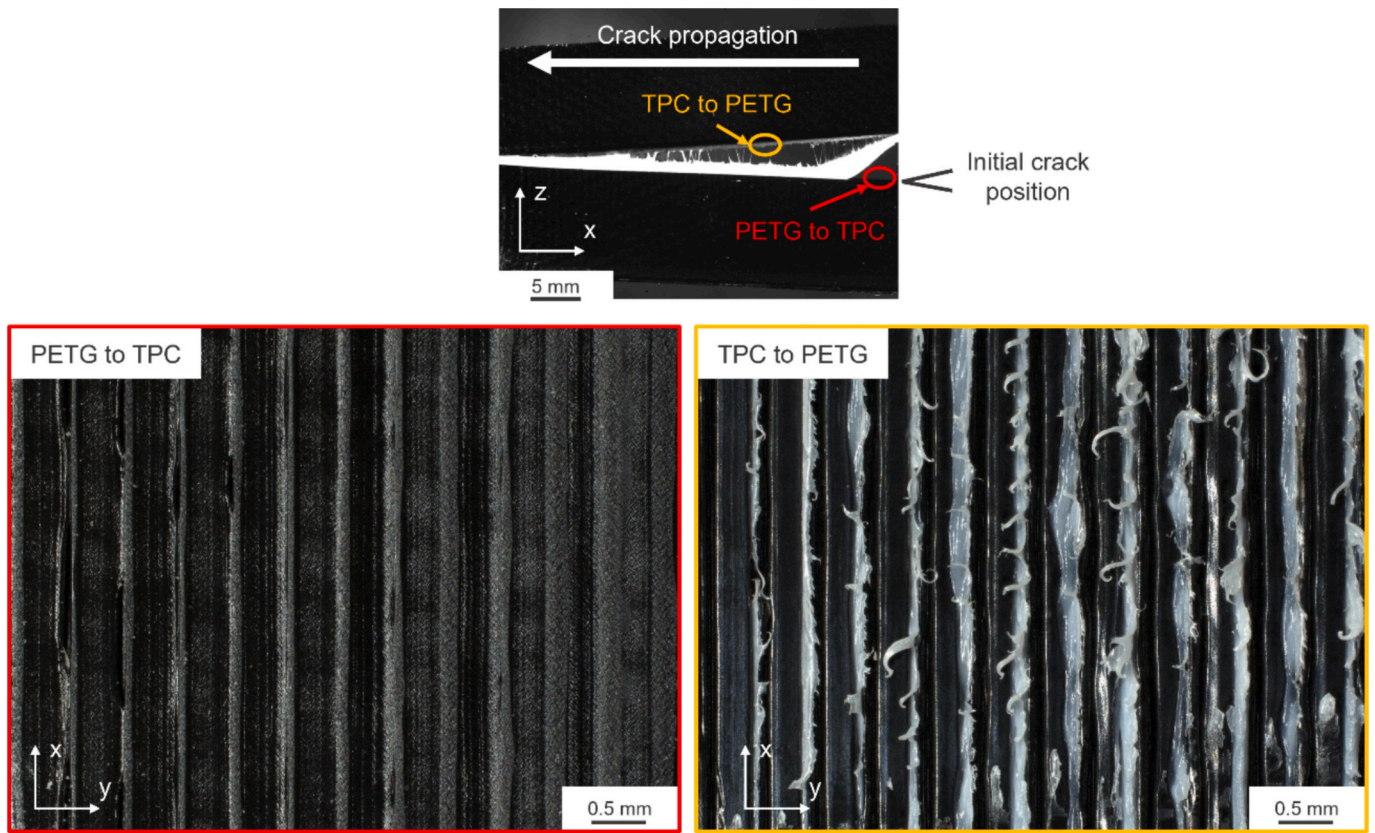
Fig. 14. Side view of the DCB sample with an IL thickness of 0.8 mm after reaching F_{max} and the resulting fracture surfaces of the two interfaces, PETG to TPC and TPC to PETG, obtained.

Table 5
Results of the interface fracture testing.

	F_{max} (N)	$F_{c, optical}$ (N)	F_c (N)	Π_i (kJ/m^2)
IL 0.3	82.4 ± 1.8	76.8 ± 1.7	74.1 ± 3.4	0.37 ± 0.04
IL 0.8	106.5 ± 7.7	95.4 ± 5.6	88.1 ± 5.2	0.61 ± 0.01

the compliant TPU layer, exhibits Π_i values ranging from approx. 0.389 ± 0.074 kJ/m^2 to 0.763 ± 0.139 kJ/m^2 [49].

3.3. Multi-material fracture testing and accuracy of failure mode prediction

In Fig. 15, the force-displacement curves from the multi-material fracture tests are presented, with one representative curve shown for each IL thickness (n = 3). The corresponding results for $F_{c, optical}$, and F_{max} are summarized in Table 6.

As evident from the force-displacement curves of both IL thicknesses, the initial response is more or less similar; however, deviations occur after reaching $F_{c, optical}$ (marked as 1) for IL 0.3 mm. The values of $F_{c, optical}$ at marking 1 differ significantly between the two IL thicknesses. Similar to the interface fracture tests, crack initiation occurs earlier for IL 0.3 mm than for IL 0.8 mm, by approx. a factor of two, which is primarily attributed to the lower Π_i. However, it is important to note that $F_{c, optical}$ from Fig. 15 and Fig. 13 are not directly comparable due to differences in the induced stress state. Regardless of IL thickness, the force continues to increase after crack initiation. Ultimately, F_{max} (Marker 2) is higher for IL 0.3 mm compared to IL 0.8 mm, before decreasing, leading to test termination at around 7 mm deformation due to the strong bending of the samples with continuous deformation. The difference in F_{max} is primarily due to the larger residual ligament in IL
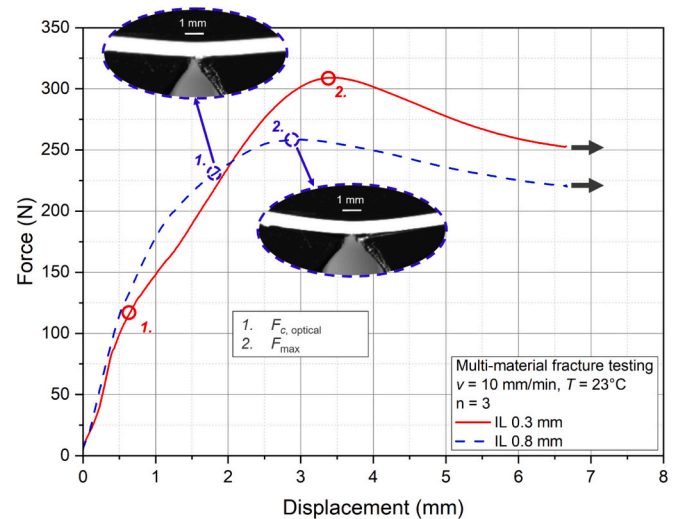

Fig. 15. Force-displacement curves from multi-material fracture testing for the two investigated IL thicknesses (0.3 and 0.8 mm). The black arrows indicate a test termination.

Table 6
Results of the multi-material fracture testing.

	F_{max} (N)	$F_{c, optical}$ (N)
IL 0.3	313.6 ± 3.8	122.3 ± 6.6
IL 0.8	259.6 ± 0.9	228.2 ± 1.3

0.3 mm. As described in the experimental section, the IL was positioned 0.4 mm away from the printed notch (PETG to TPC interface) for both thicknesses, with the IL thickness varying from this reference point. Consequently, IL 0.3 mm results in a thicker remaining ligament of the matrix material, leading to higher F_{max} values. Nevertheless, similar to the interface fracture tests, the propagation path of the crack through the specimen is of minor relevance. The critical aspect in this context remains the crack initiation step. At this point, it should be noted that the assessment of the applicability of LEFM, following the standard [72], revealed that the results, as expected, do not satisfy the linearity criterion, nor do they exhibit the formation of a sufficiently small plastic zone due to the compliant IL. The latter further indicates that the specimens used are more likely to exhibit a plane stress rather than a plane strain condition. This is of particular relevance, as the use of thicker specimens or alternative geometries with higher constraints and stress triaxiality could lead to different outcomes regarding force-displacement response and potentially failure modes [98].

Regardless of IL thickness, crack deflection, more specifically, double-sided crack deflection, was observed in all tested specimens. This phenomenon now requires evaluation based on the investigated criteria (C&G and H&H). Table 7 summarizes all relevant values necessary for calculating the ratios for the C&G and H&H criteria. Additionally, the transition values from crack deflection to crack penetration for each criterion are listed, along with an indication of whether they align with the observed crack propagation behavior in the validation specimens.

With respect to the C&G criterion, it is evident that, regardless of IL thickness, the criterion does not match the initial crack path. The calculated ratio $\sigma_i/\sigma_{m,IL}$ is approx. Twice the proposed transition value of 0.2. Consequently, the C&G criterion would predict crack penetration in the validation specimens, whereas crack deflection was observed in the experiments. This suggests that the C&G criterion may not be suitable for reliably predicting crack propagation under the given conditions.

In contrast, the H&H criterion exhibits agreement in both cases. The determined ratio for both IL thicknesses is well below the computed G_d/G_p threshold for both single-sided (0.55) and double-sided (0.38) crack deflection. This indicates that the H&H criterion seems to be more suitable for predicting failure mode than the C&G criterion. However, it should be noted that a definitive statement regarding the reliability of the determined threshold cannot be made, as the calculated ratio of Π_i/Π_{IL} falls significantly below the proposed threshold values of 0.55 and 0.38, respectively.

In previous studies [21,22], it was shown that in mono-materials, the stress-based C&G criterion consistently provided good agreement between different materials (PETG, PMMA, PLA), varying printing parameters (layer height, orientation, and print temperature), and the failure modes observed in validation specimens. A notable exception was PETG at very slow strain rates (0.1 mm/min), where no agreement was observed. The authors attributed this deviation to the increasing nonlinearity and the formation of a large plastic zone around the crack tip, which violated the fundamental assumptions of LEFM [21], for which the C&G criterion was originally developed [31]. The present study seems to confirm these assumptions. Given the high nonlinearity

coupled with the low stiffness of the specimens, the C&G criterion does not appear to be sufficient for accurate failure prediction. The H&H criterion was also investigated in a previous study [22] for different materials (PETG, PMMA, and PLA). However, unlike the C&G criterion, it did not align with the validation specimens, although the computed values were often close to the transition value. Possible reasons for this discrepancy were attributed to nonlinearity as well as the complexity of crack tip positioning. In the case of the PETG/TPC combination, where the H&H criterion appears to be valid, accurate crack positioning plays a crucial role. Unlike the C&G criterion, the H&H criterion explicitly requires that cracks initiate precisely at an interface, from where the crack either penetrates the interface and subsequent layers or deflects into the interface. In this study, this aspect was deliberately considered in the experimental setup to provide a meaningful comparison between the two criteria. The results indicate that crack tip positioning seems to be a critical factor in the applicability of the H&H criterion. However, to substantiate this observation, further validation using alternative material pairings is essential, particularly those in which the fracture mechanical properties of the bulk and the interface are more closely aligned. Due to the large disparity in the measured Π values in this study, it remains difficult to assess whether the H&H criterion can reliably predict the failure mode under the used conditions.

The key question arising from these new supplementary findings, in addition to the previously conducted studies [21,22], is how they might be utilized to predict the failure mode in FFF-printed material combinations (homogeneous and heterogeneous) based on simple characterization methods. From previous investigations, the C&G model appears to be better suited for predicting the failure mode of homogeneous material combinations, provided that the fundamental assumptions of LEFM (limited nonlinearity and small plastic zone formation around the crack tip) are fulfilled or at least closely fulfilled. Significant deviations from LEFM can lead to incorrect predictions [21,22]. Furthermore, precise crack positioning (whether at an interface or not) is of lesser importance, making the C&G criterion more applicable to real-world scenarios. Another advantage is the straightforward characterization methodology, which relies solely on simple tensile tests. The H&H criterion, on the other hand, appears to be more suitable when nonlinearities play a dominant role. However, it seems essential to ensure that the crack has already impinged on an interface, which is less representative of real-world applications. Additionally, the H&H criterion requires the use of fracture mechanics-based methods, which generally involve greater complexity and experimental effort compared to simple stress-based approaches. In both cases, it should be noted that there is no clear evidence indicating whether the transition thresholds proposed by C&G and H&H for polymeric materials accurately represent actual transition points. Consequently, their suitability for reliably predicting failure modes in such materials remains uncertain.

Finally, it is important to highlight the limitations of the applied criteria within the scope of this study. The methods investigated here are based exclusively on monotonic loading and therefore do not have general validity for fatigue, creep loading, or other time-dependent failure mechanisms. The same applies to environmental and temperature influences, which can significantly affect the mechanical behavior

Table 7
Results of the investigations carried out to predict the failure mode using C&G and H&H.

			Required values – C&G			
	IL (mm)	$\sigma_{m,IL}$ (MPa)	σ_i (MPa)	$\sigma_i/\sigma_{m,IL}$ (−)	Transition value (−)	Match (✓/✗)
C&G	0.3	17.7 ± 0.4	6.7 ± 0.3	0.38 ± 0.02	0.2	✗
	0.8					✗
			Required values – H&H			
	IL (mm)	Π_{IL} (kJ/m^2)	Π_i (kJ/m^2)	Π_i/Π_{IL} (−)	Transition value G_d/G_p (−)	Match (✓/✗)
H&H	0.3	41.5 ± 14.0	0.37 ± 0.04	0.009 ± 0.003	0.55/0.38[*]	✓
	0.8	40.1 ± 2.69	0.61 ± 0.01	0.015 ± 0.001		✓

[*] 0.55 for single and 0.38 for double deflecting cracks.

of polymeric materials. Moreover, the material selection and the interface characteristics play a crucial role in determining the failure mode. In FFF-printed structures, interface properties can be deliberately tailored through processing parameters or material selection, allowing for a certain degree of failure mode control. In contrast, multi-layered structures manufactured using traditional processing techniques often exhibit stronger interfaces than their FFF-fabricated counterparts. The failure behavior of such strongly bonded interfaces can be highly complex, as e.g. demonstrated by Wiener et al. [99] in a particle-reinforced PP/soft PP system or by Schwaiger et al. [100] in a bio-based epoxy resin system. However, to the best of the authors' knowledge, no conclusive evidence from previous studies is available on the crack deflection versus penetration phenomenon in these cases. As a result, the direct applicability of the investigated concepts is limited, and their relevance is largely confined to the PETG/TPC material combination, specifically in the context of the FFF process. As the results indicate, the properties of the two existing interfaces differ due to the manufacturing process and the varying viscosities of the materials. Consequently, the findings presented in this study are only valid once the crack has reached the PETG to TPC interface and propagates from that point under increasing load. For the upper interface, from TPC to PETG, which appears to be weaker, the values determined in this study are therefore not directly transferable.

4. Summary and conclusion

The investigations presented in this study aim to evaluate the applicability of two established criteria from the literature, those proposed by Cook & Gordon (C&G) and He & Hutchinson (H&H), for predicting the failure mode of multi-material structures produced via fused filament fabrication (FFF). Glycol-modified poly(ethylene terephthalate) (PETG) was used as the stiff matrix material, while a compliant thermoplastic elastomer based on copolyester (TPC) served as the interlayer (IL). Two different IL thicknesses, 0.3 and 0.8 mm, were examined. To assess the C&G criterion, tensile strengths of both mono-material and multi-material specimens were measured to determine the strength of the mono-materials (σ_m) and interface strength (σ_i) in the multi-material configuration. For the H&H criterion, the for the prediction required material parameters were obtained using two approaches: the essential work of fracture (EWF) method to determine the IL fracture toughness (Π_{IL}), and a stiffness drop technique combined with a finite element model employing the J-integral method to quantify the interface fracture (Π_i) toughness between PETG and TPC. The validation of the results was ultimately performed using single-edge notched bending (SENB) specimens. However, it should be noted that this study does not aim to provide an extensive material characterization but rather focuses on evaluating the suitability of the two criteria for failure mode prediction, for which the extent of the investigations is deemed sufficient.

The mono-material tensile tests revealed that the two materials exhibit distinctly different deformation behaviors. The matrix material exhibited higher stiffness and strength, along with a yield point and cold drawing behavior, while the IL material exhibits a hyperelastic response typical of thermoplastic elastomers, with lower stiffness and strength, but substantially higher elongation at break. For the determination of σ_i, two different approaches (Approach 1 and Approach 2) were applied. In Approach 1, the compliant IL was printed between layers of the matrix material. In Approach 2, bi-layer specimens were produced, containing only a single interface. The results indicate that Approach 1 is unsuitable for a reliable evaluation of σ_i, as it was prone to out-of-plane failure mechanisms arising from process-induced effects and a notable viscosity mismatch between the materials. In contrast, Approach 2 yielded consistent interfacial failure, allowing for the extraction of a representative σ_i value. The results for determining Π_{IL} using the EWF method indicate an independence of the IL thickness. Conversely, Π_i seems to exhibit a dependence on IL thickness at least on a macroscopic scale,

with increasing values observed at higher thicknesses. This behavior was primarily attributed to the enlargement of the process zone around the crack tip, which facilitates increased energy dissipation during the crack initiation process.

Overall, the findings revealed that the C&G criteria do not accurately predict the observed failure behavior under the given conditions. Despite being widely applicable to homogeneous polymeric materials in previous studies [21,22], its stress-based formulation does not account for the significant nonlinearity coupled with eventually large plastic zone sizes present in the PETG/TPC system, resulting in incorrect failure mode predictions. Addressing this challenge through innovative approaches, such as the "equivalent material concept" [101] or the "fictitious material concept" [102] could be a promising direction for future work. These methods may enhance the predictive capability for material combinations whose properties deviate significantly from linear-elastic behavior. However, in contrast to the C&G criteria, the H&H criteria showed good agreement with the experimental observations. For both IL thicknesses, the computed toughness ratio (Π_i/Π_{IL}) remained well below the theoretical thresholds for crack deflection/penetration. However, due to the pronounced mismatch in fracture properties and the considerable deviation from the proposed threshold, the general applicability of the H&H criteria remains uncertain. Nevertheless, its foundation in fracture mechanics offers a more realistic representation of real-world failure behavior compared to the strength-based method, provided that the challenge of precise crack tip positioning at the interface is properly addressed.

For the sake of completeness, both criteria are limited in scope. Their applicability is confined to monotonic loading and does not extend to fatigue, creep, or environmental effects. Furthermore, bonding strength in FFF structures is highly dependent on process parameters and material selection, and may differ significantly from conventionally manufactured multi-layered systems. Furthermore, the question arises regarding the transferability of the concepts from a specimen level to a real component, which at the very least requires comparable stress states in order to ensure reliability in practical application. As shown, several open questions remain at this stage that should be addressed in future works to improve the understanding of crack deflection and penetration in polymeric materials. To date, the validity of the presented results is limited to the PETG/TPC material combination.

CRediT authorship contribution statement

Christoph Waly: Writing – original draft, Validation, Methodology, Investigation, Conceptualization, Visualization. **Vasco D.C. Pires:** Writing – review & editing, Validation, Formal analysis, Investigation. **Philipp Beier:** Writing – review & editing, Resources, Validation. **Sandra Schulnig:** Writing – review & editing, Conceptualization, Methodology. **Ivica Duretek:** Writing – review & editing, Methodology, Validation. **Martin Pletz:** Writing – review & editing, Formal analysis, Investigation. **Florian Arbeiter:** Writing – review & editing, Supervision, Methodology, Conceptualization, Resources.

Declaration of competing interest

The authors declare that they have no known competing financial interests or personal relationships that could have appeared to influence the work reported in this paper.

Acknowledgement

Appendix A

A.1. Melt flow rate (MFR) determination

The MFR of both materials, PETG and TPC, was measured using a CEAST Modular Melt Flow Tester, model 7023.003 (CEAST S.p.A., Italy), following EN ISO 1133-1:2022, Method A [103]. Prior to testing, the filaments were cut into approx. 5 mm long pieces, pre-dried as described in Section 2.1, and then placed into the preheated barrel of the extrusion plastometer at 240 °C, corresponding to the nozzle temperature used in the FFF process. The material was compacted and conditioned for 4 min. After preheating, a 2.16 kg load was applied on top of the piston. The mass of individual extrudates, extruded through a standard die with a length of 8 mm and an internal diameter of 2.095 mm, was measured using an AG204DR analytical balance (Mettler Toledo GmbH, Austria). The reported MFR values are expressed in g/10 min and represent the average of at least five measurements.

An MFR of 10.6 ± 0.6 g/10 min was determined for PETG, whereas a significantly higher MFR of 84.0 ± 1.4 g/10 min was measured for TPC. These differences in MFR indicate a disparity in viscosity and, consequently, in the flow behavior of the two materials under comparable processing conditions during strand deposition in FFF. The lower viscosity of TPC suggests enhanced wetting behavior during filament deposition, regardless of whether the previously deposited strand material is similar (TPC) or dissimilar (PETG).

A.2. Porosity determination

To gain insights into the actual cross-sectional area of the printed specimens, density measurements were performed according to Archimedes' principle, as specified in DIN EN ISO 1183 [104]. The measurements were carried out using a laboratory balance (AG 204 Delta Range, Mettler-Toledo AG, Switzerland) with distilled water as immersion fluid. Based on the measured densities, the porosity was then calculated using Eq. (A1):

$$Porosity\ in\% = \frac{\rho_{Filament} - \rho_{FFF}}{\rho_{Filament}} \bullet 100\% \tag{A1}$$

where $\rho_{Filament}$ represents the density of the neat PETG/TPC filament, and ρ_{FFF} corresponds to the density of a printed structure. For this purpose, specimens of approx. $(5 \times 10 \times 6)$ mm^3 were extracted from the tensile test specimens described in Section 2.3.2 (Approach 2), for both PETG and TPC. In total, three measurements were conducted for each filament and each printed PETG/TPC structure.

Under the printing conditions described in Section 2.2, the porosity was determined to be approx. 4.0 ± 0.5 % for PETG and 1.0 ± 0.1 % for TPC. The PETG result is in good agreement with previous measurements reported in Ref. [22]. The low porosity of TPC can essentially be explained by its high MFR and the associated low viscosity, which promotes during the strand deposition a more homogeneous and denser structure.

Data availability

Data will be made available on request.

References

[1] C.G. Amza, A. Zapciu, G. Constantin, F. Baciu, M.I. Vasile, Enhancing mechanical properties of polymer 3D printed parts, Polymers (Basel) 13 (2021), https://doi.org/10.3390/polym13040562.

[2] M. Bergoglio, E. Rossegger, S. Schlögl, T. Griesser, C. Waly, F. Arbeiter, M. Sangermano, Multi-material 3D printing of biobased epoxy resins, Polymers (Basel) 16 (2024), https://doi.org/10.3390/polym16111510.

[3] F. Górski, W. Kuczko, W. Weiss, R. Wichniarek, M. Żukowska, Prototyping of an individualized multi-material wrist orthosis using fused deposition modelling, Adv. Sci. Technol. Res. J. 13 (2019) 39–47, https://doi.org/10.12913/22998624/113543.

[4] D. Han, H. Lee, Recent advances in multi-material additive manufacturing: methods and applications, Curr. Opin. Chem. Eng. 28 (2020) 158–166, https://doi.org/10.1016/j.coche.2020.03.004.

[5] F.-H. Wang, C.-Y. You, N. Tian, H.-G. Liu, J. Zhang, X.-P. Zhu, 3D printing of soft magnetic materials: from printing to applications, J. Alloys Compd. 990 (2024) 174486, https://doi.org/10.1016/j.jallcom.2024.174486.

[6] A. Tariq, Z.U. Arif, M.Y. Khalid, M. Hossain, P.I. Rasool, R. Umer, S. Ramakrishna, Recent advances in the additive manufacturing of stimuli-responsive soft polymers, Adv. Eng. Mater. 25 (2023) 2301074, https://doi.org/10.1002/adem.202301074.

[7] S. Pahari, G.W. Melenka, Analysis of the interface properties of multi-material fused filament fabricated (FFF) printed polymer composite structures, Int. J. Adhes. Adhes. 142 (2025) 104074, https://doi.org/10.1016/j.ijadhadh.2025.104074.

[8] R. Velu, R. Sathishkumar, A. Saiyathibrahim, I.V. Shishkovsky, Perspective chapter: multi-material in 3D printing for engineering applications, in: Advanced Additive Manufacturing, IntechOpen, 2022.

[9] M. Lalegani Dezaki, R. Sales, A. Zolfagharian, H. Yazdani Nezhad, M. Bodaghi, Soft pneumatic actuators with integrated resistive sensors enabled by multi-material 3D printing, Int. J. Adv. Manuf. Technol. 128 (2023) 4207–4221, https://doi.org/10.1007/s00170-023-12181-8.

[10] G.L. Goh, H. Zhang, T.H. Chong, W.Y. Yeong, 3D Printing of Multilayered and Multimaterial Electronics: A Review, Adv Elect Materials 7 (2021) 2100445. https://doi.org/10.1002/aelm.202100445.

[11] A. Chen, W. Wang, Z. Mao, Y. He, S. Chen, G. Liu, J. Su, P. Feng, Y. Shi, C. Yan, J. Lu, Multimaterial 3D and 4D bioprinting of Heterogenous constructs for tissue engineering, Adv. Mater. 36 (2024) e2307686, https://doi.org/10.1002/adma.202307686.

[12] C. Waly, S. Petersmann, F. Arbeiter, Multimaterial extrusion-based additive manufacturing of compliant crack arrester: influence of interlayer length, thickness, and applied strain rate, Adv. Eng. Mater. (2022) 2101703, https://doi.org/10.1002/adem.202101703.

[13] F. Libonati, G.X. Gu, Z. Qin, L. Vergani, M.J. Buehler, Bone-inspired materials by design: toughness amplification observed using 3D printing and testing, Adv. Eng. Mater. 18 (2016) 1354–1363, https://doi.org/10.1002/adem.201600143.

[14] A. Ingrole, T.G. Aguirre, L. Fuller, S.W. Donahue, Bioinspired energy absorbing material designs using additive manufacturing, J. Mech. Behav. Biomed. Mater. 119 (2021) 104518, https://doi.org/10.1016/j.jmbbm.2021.104518.

[15] F.J. Arbeiter, S. Petersmann, J. Wiener, F. Oesterreicher, M. Spoerk, G. Pinter, Using compliant interlayers as crack arresters in 3-D-printed polymeric structures, Mater. Perform. Charact. 9 (2020) 688–700, https://doi.org/10.1520/MPC20190201.

[16] I. Khan, I. Barsoum, M. Abas, A. Al Rashid, M. Koç, M. Tariq, A review of extrusion-based additive manufacturing of multi-materials-based polymeric laminated structures, Compos. Struct. 349-350 (2024) 118490, https://doi.org/10.1016/j.compstruct.2024.118490.

[17] A. Nazir, O. Gokcekaya, K. Md Masum Billah, O. Ertugrul, J. Jiang, J. Sun, S. Hussain, Multi-material additive manufacturing: a systematic review of design, properties, applications, challenges, and 3D printing of materials and cellular metamaterials, Mater. Des. 226 (2023) 111661, https://doi.org/10.1016/j.matdes.2023.111661.

[18] J.E. Seppala, K.D. Migler, Infrared thermography of welding zones produced by polymer extrusion additive manufacturing, Addit. Manuf. 12 (2016) 71–76, https://doi.org/10.1016/j.addma.2016.06.007.

[19] Babak Kianian, Wohlers Report 2016: 3D Printing and Additive Manufacturing State of the Industry, Annual Worldwide Progress Report: Chapter Title: The Middle East, 2016.

[20] Y. Tao, F. Kong, Z. Li, J. Zhang, X. Zhao, Q. Yin, D. Xing, P. Li, A review on voids of 3D printed parts by fused filament fabrication, J. Mater. Res. Technol. 15 (2021) 4860–4879, https://doi.org/10.1016/j.jmrt.2021.10.108.

[21] C. Waly, S. Schulnig, F. Arbeiter, Strain rate-dependent failure modes of material extrusion-based additively manufactured PETG: a study on crack deflection and penetration, Theor. Appl. Fract. Mech. 136 (2025) 104834, https://doi.org/10.1016/j.tafmec.2024.104834.

[22] C. Waly, S. Petersmann, F. Arbeiter, Crack penetration versus deflection in extrusion-based additive manufacturing – impact of nozzle temperature and morphology, Theor. Appl. Fract. Mech. 127 (2023) 104032, https://doi.org/10.1016/j.tafmec.2023.104032.

[23] D. Martínez, V. Gupta, Energy criterion for crack deflection at an interface between two orthotropic media, J. Mech. Phys. Solids 42 (1994) 1247–1271, https://doi.org/10.1016/0022-5096(94)90034-5.

[24] D. Leguillon, C. Lacroix, E. Martin, Interface debonding ahead of a primary crack, J. Mech. Phys. Solids 48 (2000) 2137–2161, https://doi.org/10.1016/S0022-5096(99)00101-5.

[25] M.Y. He, J.W. Hutchinson, Crack deflection at an interface between dissimilar elastic materials, Int. J. Solids Struct. 1989 (1989) 1053–1067.

[26] M. He, C. Hsueh, P. Becher, Deflection versus penetration of a wedge-loaded crack: effects of branch-crack length and penetrated-layer width, Compos. Part B Eng. 31 (2000) 299–308, https://doi.org/10.1016/S1359-8368(00)00007-X.

[27] X. Gao, S. Qi, X. Kuang, Y. Su, J. Li, D. Wang, Fused filament fabrication of polymer materials: a review of interlayer bond, Addit. Manuf. 37 (2021) 101658, https://doi.org/10.1016/j.addma.2020.101658.

[28] S. Hasanov, A. Gupta, A. Nasirov, I. Fidan, Mechanical characterization of functionally graded materials produced by the fused filament fabrication process, J. Manuf. Process. 58 (2020) 923–935, https://doi.org/10.1016/j.jmapro.2020.09.011.

[29] D. Dairabayeva, A. Perveen, D. Talamona, Investigation on the mechanical performance of mono-material vs multi-material interface geometries using fused filament fabrication, RPJ 29 (2023) 40–52, https://doi.org/10.1108/RPJ-07-2022-0221.

[30] R. Freund, H. Watschke, J. Heubach, T. Vietor, Determination of influencing factors on Interface strength of additively manufactured multi-material parts by material extrusion, Appl. Sci. 9 (2019) 1782, https://doi.org/10.3390/app9091782.

[31] John Cook, Jesse E. Gordon, A mechanism for the control of crack propagation in all-brittle systems, Proc. R. Soc. Lond. Ser. A 282 (1964) 508–520.

[32] M.Y. He, A.G. Evans, J.W. Hutchinson, Crack deflection at an interface between dissimilar elastic materials: role of residual stresses, Int. J. Solids Struct. 31 (1994) 3443–3455, https://doi.org/10.1016/0020-7683(94)90025-6.

[33] P.F. Becher, E.Y. Sun, C.-H. Hsueh, K.B. Alexander, S.-L. Hwang, S.B. Waters, C.G. Westmoreland, Debonding of interfaces between beta-silicon nitride whiskers and Si-Al-Y oxynitride glasses, Acta Mater. 44 (1996) 3881–3893, https://doi.org/10.1016/S1359-6454(96)00069-9.

[34] R. Bermejo, Failure resistance optimisation in layered ceramics designed with strong, Interfaces (2010) 15–20, https://doi.org/10.4416/JCST2010-00007.

[35] R. Bermejo, R. Danzer, High failure resistance layered ceramics using crack bifurcation and interface delamination as reinforcement mechanisms, Eng. Fract. Mech. 77 (2010) 2126–2135, https://doi.org/10.1016/j.engfracmech.2010.02.020.

[36] K. Madani, M. Belhouari, B. Bachir Bouiadjra, B. Serier, M. Benguediab, Crack deflection at an interface of alumina/metal joint: a numerical analysis, Comput. Mater. Sci. 38 (2007) 625–630, https://doi.org/10.1016/j.commatsci.2006.04.006.

[37] W. Lee, S.J. Howard, W.J. Clegg, Growth of interface defects and its effect on crack deflection and toughening criteria, Acta Mater. 44 (1996) 3905–3922, https://doi.org/10.1016/S1359-6454(96)00068-7.

[38] M. Alam, J.P. Parmigiani, J.J. Kruzic, An experimental assessment of methods to predict crack deflection at an interface, Eng. Fract. Mech. 181 (2017) 116–129, https://doi.org/10.1016/j.engfracmech.2017.05.013.

[39] Z. Jia, L. Wang, 3D printing of biomimetic composites with improved fracture toughness, Acta Mater. 173 (2019) 61–73, https://doi.org/10.1016/j.actamat.2019.04.052.

[40] Y.F. Lam, T. Abdullah, K. Kirane, Dynamic crack penetration vs. deflection at material interfaces and the role of rate dependent strength and toughness, J. Mech. Phys. Solids 173 (2023) 105208, https://doi.org/10.1016/j.jmps.2023.105208.

[41] E. Jungstedt, M. Da Vinícius Tavares, S. Costa, L.A. Berglund Östlund, On the high fracture toughness of wood and polymer-filled wood composites – crack deflection analysis for materials design, Eng. Fract. Mech. 300 (2024) 109994, https://doi.org/10.1016/j.engfracmech.2024.109994.

[42] M. Ju, D. Wang, J. Shi, J. Li, Q. Yao, X. Li, Physical and numerical investigations on bedding adhesion strength on stratified rock roof fracture with longwall coal mining, Geomech. Geophys. Geoenerg. Georesour. 7 (2021), https://doi.org/10.1007/s40948-020-00209-2.

[43] J. Yin, C. Lu, J. Fu, Y. Huang, Y. Zheng, Interfacial bonding during multi-material fused deposition modeling (FDM) process due to inter-molecular diffusion, Mater. Des. 150 (2018) 104–112, https://doi.org/10.1016/j.matdes.2018.04.029.

[44] L.R. Lopes, A.F. Silva, O.S. Carneiro, Multi-material 3D printing: the relevance of materials affinity on the boundary interface performance, Addit. Manuf. 23 (2018) 45–52, https://doi.org/10.1016/j.addma.2018.06.027.

[45] F. Richter, D. Wu, Interfacial adhesion between dissimilar thermoplastics fabricated via material extrusion-based multi-material additive manufacturing, Mater. Des. 252 (2025) 113688, https://doi.org/10.1016/j.matdes.2025.113688.

[46] D. Yavas, Q. Liu, Z. Zhang, D. Wu, Design and fabrication of architected multi-material lattices with tunable stiffness, strength, and energy absorption, Mater. Des. 217 (2022) 110613, https://doi.org/10.1016/j.matdes.2022.110613.

[47] M.F. Rabbi, V. Chalivendra, Interfacial fracture characterization of multi-material additively manufactured polymer composites, Compos. Part C: Open Access 5 (2021) 100145, https://doi.org/10.1016/j.jcomc.2021.100145.

[48] T. Stiller, R.C. Kerschbaumer, C. Waly, B. Zink, J. Slapnik, G. Pinter, Investigating the influence of bending stiffness and processing parameters on single-leg bending geometries of additively manufactured composites, Results Eng. 24 (2024) 103276, https://doi.org/10.1016/j.rineng.2024.103276.

[49] A.S. Pakhare, K. Kalia, S.P.V. Nadimpalli, A. Ameli, Interface fracture characterization of 3D-printed rigid/flexible dissimilar polymers, Prog. Addit. Manuf. 9 (2024) 2235–2247, https://doi.org/10.1007/s40964-024-00575-3.

[50] M.R. Khosravani, P. Soltani, T. Reinicke, Fracture and structural performance of adhesively bonded 3D-printed PETG single lap joints under different printing parameters, Theoretical and Applied Fracture Mechanics 116 (2021) 103087, https://doi.org/10.1016/j.tafmec.2021.103087.

[51] K. Durgashyam, M. Indra Reddy, A. Balakrishna, K. Satyanarayana, Experimental investigation on mechanical properties of PETG material processed by fused deposition modeling method, Materials Today: Proceedings 18 (2019) 2052–2059. https://doi.org/10.1016/j.matpr.2019.06.082.

[52] S. Guessasma, S. Belhabib, H. Nouri, Printability and Tensile Performance of 3D Printed Polyethylene Terephthalate Glycol Using Fused Deposition Modelling, Polymers (Basel) 11 (2019) 1220. https://doi.org/10.3390/polym11071220.

[53] S. Kasmi, G. Ginoux, S. Allaoui, S. Alix, Investigation of 3D printing strategy on the mechanical performance of coextruded continuous carbon fiber reinforced PETG, J Appl Polym Sci 138 (2021) 50955. https://doi.org/10.1002/app.50955.

[54] Prusa Research a.s., Prusament PETG - Technisches Datenblatt. https://www.prusa3d.com/de/produkt/prusament-petg-jet-black-1kg/ (accessed 24 April 2023).

[55] FormFutura, FlexiFil TPC - Technical Datasheet, https://www.3dmensionals.de/formfutura-flexifil-flexibles-tpc-special-filament (accessed 27 March 2025).

[56] X. Gao, S. Qi, D. Zhang, Y. Su, D. Wang, The role of poly (ethylene glycol) on crystallization, interlayer bond and mechanical performance of polylactide parts fabricated by fused filament fabrication, Addit. Manuf. 35 (2020) 101414, https://doi.org/10.1016/j.addma.2020.101414.

[57] DIN EN ISO 527-2:2012–06, Kunststoffe - Bestimmung der Zugeigenschaften - Teil_2: Prüfbedingungen für Form- und Extrusionsmassen (ISO_527–2:2012); Deutsche Fassung EN_ISO_527–2:2012, Beuth Verlag GmbH, Berlin.

[58] A. Sola, W.J. Chong, D. Pejak Simunec, Y. Li, A. Trinchi, I. Kyratzis, C. Wen, Open challenges in tensile testing of additively manufactured polymers: a literature survey and a case study in fused filament fabrication, Polym. Test. 117 (2023) 107859, https://doi.org/10.1016/j.polymertesting.2022.107859.

[59] V. Gupta, A.S. Argon, Z. Suo, Crack deflection at an Interface between two Orthotopic media, J. Appl. Mech. 59 (1992) S79–S87, https://doi.org/10.1115/1.2899511.

[60] DIN EN ISO 7500-1:2018-06, Metallische Werkstoffe -Kalibrierung und Überprüfung von statischen einachsigen Prüfmaschinen -Teil_1: Zug- und Druckprüfmaschinen -Kalibrierung und Überprüfung der Kraftmesseinrichtung (ISO_7500-1:2018); Deutsche Fassung EN_ISO_7500-1:2018, DIN Media GmbH, Berlin.

[61] DIN EN ISO 9513:2013–05, Metallische Werkstoffe - Kalibrierung von Längenänderungs-Messeinrichtungen für die Prüfung mit einachsiger Beanspruchung (ISO_9513:2012_+_Cor._1:2013); Deutsche Fassung EN_ISO_9513: 2012, DIN Media GmbH, Berlin.

[62] W. Lee, Y.-H. Yoo, H. Shin, Reconsideration of crack deflection at planar interfaces in layered systems, Compos. Sci. Technol. 64 (2004) 2415–2423, https://doi.org/10.1016/j.compscitech.2004.05.011.

[63] J. Dundurs, Discussion: "edge-bonded dissimilar orthogonal elastic wedges under Normal and shear loading" (Bogy, D. B., 1968, ASME J. Appl. Mech., 35, pp. 460–466), J. Appl. Mech. 36 (1969) 650–652, https://doi.org/10.1115/1.3564739.

[64] International Standard, Plastics — Determination of fracture toughness of films and thin sheets — Essential work of fracture (EWF) method, 2022nd ed. https://www.iso.org/standard/75907.html.

[65] K.B. Broberg, Crack-growth criteria and non-linear fracture mechanics, J. Mech. Phys. Solids 19 (1971) 407–418, https://doi.org/10.1016/0022-5096(71)90008-1.

[66] K.B. Broberg, On stable crack growth, J. Mech. Phys. Solids 23 (1975) 215–237, https://doi.org/10.1016/0022-5096(75)90017-4.

[67] Y.W. Mai, B. Cotterell, The essential work of fracture for tearing of ductile metals, Int. J. Fract. 24 (1984) 229–236, https://doi.org/10.1007/BF00032685.

[68] Y.-W. Mai, B. Cotterell, On the essential work of ductile fracture in polymers, Int. J. Fract. 32 (1986) 105–125, https://doi.org/10.1007/BF00019787.

[69] Y.-W. Mai, P. Powell, Essential work of fracture and j-integral measurements for ductile polymers, J. Polym. Sci. B Polym. Phys. 29 (1991) 785–793, https://doi.org/10.1002/polb.1991.090290702.

[70] J.R. Rice, A path independent integral and the approximate analysis of strain concentration by notches and cracks, J. Appl. Mech. 35 (1968) 379–386, https://doi.org/10.1115/1.3601206.

[71] N. Aliheidari, R. Tripuraneni, A. Ameli, S. Nadimpalli, Fracture resistance measurement of fused deposition modeling 3D printed polymers, Polym. Test. 60 (2017) 94–101, https://doi.org/10.1016/j.polymertesting.2017.03.016.

[72] D20 Committee, Test Methods for Plane-Strain Fracture Toughness and Strain Energy Release Rate of Plastic Materials, ASTM International, West Conshohocken, PA.

[73] C.-H. Liu, Y. Chen, S.-Y. Yang, Quantification of hyperelastic material parameters for a 3D-printed thermoplastic elastomer with different infill percentages, Mater Today Commun 26 (2021) 101895, https://doi.org/10.1016/j.mtcomm.2020.101895.

[74] S. Wang, Y. Ma, Z. Deng, S. Zhang, J. Cai, Effects of fused deposition modeling process parameters on tensile, dynamic mechanical properties of 3D printed polylactic acid materials, Polym. Test. 86 (2020) 106483, https://doi.org/10.1016/j.polymertesting.2020.106483.

[75] T.J. Coogan, D.O. Kazmer, Modeling of interlayer contact and contact pressure during fused filament fabrication, J. Rheol. 63 (2019) 655–672, https://doi.org/10.1122/1.5093033.

[76] X. Tian, T. Liu, C. Yang, Q. Wang, D. Li, Interface and performance of 3D printed continuous carbon fiber reinforced PLA composites, Compos. A: Appl. Sci. Manuf. 88 (2016) 198–205, https://doi.org/10.1016/j.compositesa.2016.05.032.

[77] P. Wang, B. Zou, H. Xiao, S. Ding, C. Huang, Effects of printing parameters of fused deposition modeling on mechanical properties, surface quality, and microstructure of PEEK, J. Mater. Process. Technol. 271 (2019) 62–74, https://doi.org/10.1016/j.jmatprotec.2019.03.016.

[78] P. Cunha, R. Teixeira, O.S. Carneiro, A.F. Silva, Multi-material fused filament fabrication: an expedited methodology to assess the affinity between different materials, Prog. Addit. Manuf. 8 (2023) 195–204, https://doi.org/10.1007/s40964-022-00322-6.

[79] E.M. Hunt, Mechanical Engineering Education: Preschool To Graduate School, IntechOpen, [s.l.], 2012.

[80] H. Rezayat, W. Zhou, A. Siriruk, D. Penumadu, S.S. Babu, Structure–mechanical property relationship in fused deposition modelling, Mater. Sci. Technol. 31 (2015) 895–903, https://doi.org/10.1179/1743284715Y.0000000010.

[81] M. Rink, L. Andena, C. Marano, The essential work of fracture in relation to J-integral, Eng. Fract. Mech. 127 (2014) 46–55, https://doi.org/10.1016/j.engfracmech.2014.05.006.

[82] P. Verma, J. Ubaid, A. Schiffer, A. Jain, E. Martínez-Pañeda, S. Kumar, Essential work of fracture assessment of acrylonitrile butadiene styrene (ABS) processed via fused filament fabrication additive manufacturing, Int. J. Adv. Manuf. Technol. 113 (2021) 771–784, https://doi.org/10.1007/s00170-020-06580-4.

[83] M. Lorenzo-Bañuelos, A. Díaz, I.I. Cuesta, Influence of raster orientation on the determination of fracture properties of polypropylene thin components produced by additive manufacturing, Theor. Appl. Fract. Mech. 107 (2020) 102536, https://doi.org/10.1016/j.tafmec.2020.102536.

[84] Y. Zhang, H. Ye, L. Yuan, C. Luo, X. Ren, Q. Yu, J. Chen, Q. Gao, Y. Lei, Y. Cheng, A. Sun, G. Xu, J. Guo, The effect of weak interface on the fracture behavior of material extrusion 3D-printed polyetherimide, Appl. Mater. Today 34 (2023) 101905, https://doi.org/10.1016/j.apmt.2023.101905.

[85] M. Maspoch, V. Hénault, D. Ferrer-Balas, J. Velasco, O. Santana, Essential work of fracture on PET films: influence of the thickness and the orientation, Polym. Test. 19 (2000) 559–568, https://doi.org/10.1016/S0142-9418(99)00026-4.

[86] G. Sharma, A. Vuppuluri, K. Suresh, Essential work of fracture studies of 3D printed PEEK (poly-ether-ether-ketone) polymer, Eng. Fract. Mech. 271 (2022) 108656, https://doi.org/10.1016/j.engfracmech.2022.108656.

[87] T. Bárány, T. Czigány, J. Karger-Kocsis, Application of the essential work of fracture (EWF) concept for polymers, related blends and composites: a review, Prog. Polym. Sci. 35 (2010) 1257–1287, https://doi.org/10.1016/j.progpolymsci.2010.07.001.

[88] J.-M. Lee, B.-H. Choi, J.-S. Moon, E.-S. Lee, Determination of the tear properties of thermoplastic polyester elastomers (TPEEs) using essential work of fracture (EWF) test method, Polym. Test. 28 (2009) 854–865, https://doi.org/10.1016/j.polymertesting.2009.07.008.

[89] U. Altuntas, D. Coker, D. Yavas, Creating tougher interfaces via suture morphology in 3D-printed multi-material polymer composites by fused filament fabrication, Addit. Manuf. 61 (2023) 103359, https://doi.org/10.1016/j.addma.2022.103359.

[90] J. Kluczyński, L. Śnieżek, A. Kravcov, K. Grzelak, P. Svoboda, I. Szachogłuchowicz, O. Franek, N. Morozov, J. Torzewski, P. Kubeček, The examination of restrained joints created in the process of multi-material FFF additive manufacturing technology, Materials 13 (2020) 903, https://doi.org/10.3390/ma13040903.

[91] N. Yu, G. Jing, J. Yang, Z. Wang, Q. Zhang, J. Li, Effects of a rotary shear field on the interlayer bond and mechanical properties of polylactide fabricated using fused filament fabrication, Polym. Test. 116 (2022) 107805, https://doi.org/10.1016/j.polymertesting.2022.107805.

[92] S. Sharafi, M.H. Santare, J. Gerdes, S.G. Advani, A review of factors that influence the fracture toughness of extrusion-based additively manufactured polymer and polymer composites, Addit. Manuf. 38 (2021) 101830, https://doi.org/10.1016/j.addma.2020.101830.

[93] E.A. Papon, A. Haque, Tensile properties, void contents, dispersion and fracture behaviour of 3D printed carbon nanofiber reinforced composites, J. Reinf. Plast. Compos. 37 (2018) 381–395, https://doi.org/10.1177/0731684417750477.

[94] U. Altuntas, D. Coker, D. Yavas, Bioinspired soft-hard interfaces fabricated by multi-material additive manufacturing: a fracture mechanics investigation using essential work of fracture, Mech. Mater. 195 (2024) 105035, https://doi.org/10.1016/j.mechmat.2024.105035.

[95] M.D. Banea, L.F.M. Da Silva, R.D.S.G. Campilho, The effect of adhesive thickness on the mechanical behavior of a structural polyurethane adhesive, J. Adhes. 91 (2015) 331–346, https://doi.org/10.1080/00218464.2014.903802.

[96] S. Azari, M. Papini, J.K. Spelt, Effect of adhesive thickness on fatigue and fracture of toughened epoxy joints – part I: experiments, Eng. Fract. Mech. 78 (2011) 153–162, https://doi.org/10.1016/j.engfracmech.2010.06.025.

[97] A. Salazar, J. Rodríguez, F. Arbeiter, G. Pinter, A.B. Martínez, Fracture toughness of high density polyethylene: fatigue pre-cracking versus femtolaser, razor sharpening and broaching, Eng. Fract. Mech. 149 (2015) 199–213, https://doi.org/10.1016/j.engfracmech.2015.07.016.

[98] T.L. Anderson. Fracture mechanics: Fundamentals and applications, third. ed., CRC Taylor & Francis, Boca Raton, 2005.

[99] J. Wiener, F. Arbeiter, O. Kolednik, G. Pinter, Influence of layer architecture on fracture toughness and specimen stiffness in polymer multilayer composites, Mater. Des. 219 (2022) 110828, https://doi.org/10.1016/j.matdes.2022.110828.

[100] M. Schwaiger, C. Waly, M. Huszar, G. Oreski, M. Feuchter, F. Arbeiter, K. Resch-Fauster, Bioinspired fracture toughness enhancement of a fully bio-based epoxy resin, Polym. Test. 124 (2023) 108098, https://doi.org/10.1016/j.polymertesting.2023.108098.

[101] A.R. Torabi, Estimation of tensile load-bearing capacity of ductile metallic materials weakened by a V-notch: the equivalent material concept, Mater. Sci. Eng. A 536 (2012) 249–255, https://doi.org/10.1016/j.msea.2012.01.007.

[102] A.R. Torabi, M. Kamyab, The fictitious material concept, Eng. Fract. Mech. 209 (2019) 17–31, https://doi.org/10.1016/j.engfracmech.2019.01.022.

[103] ÖNORM EN ISO 1133-1:2022, Kunststoffe - Bestimmung der Schmelze-Massefließrate (MFR) und der Schmelze-Volumenfließrate (MVR) von Thermoplasten - Teil 1: Allgemeines Prüfverfahren (ISO 1133-1:2022), Austrian Standard International. https://www.austrian-standards.at.

[104] DIN EN ISO 1183-1:2019-09, Kunststoffe -Verfahren zur Bestimmung der Dichte von nicht verschäumten Kunststoffen - Teil 1: Eintauchverfahren, Verfahren mit Flüssigkeitspyknometer und Titrationsverfahren (ISO 1183-1:2019, korrigierte Fassung 2019-05); Deutsche Fassung EN ISO 1183-1:2019, Beuth Verlag GmbH, Berlin.